

Galactic wormholes: Geometry, stability, and echoesShauvik Biswas^{1,*}, Chiranjeeb Singha^{2,†} and Sumanta Chakraborty^{1,‡}¹*School of Physical Sciences, Indian Association for the Cultivation of Science, Kolkata 700032, India*²*Theory Division, Saha Institute of Nuclear Physics, Kolkata 700064, India*

(Received 28 July 2023; accepted 22 February 2024; published 14 March 2024)

In this work, we present the environmental effects on wormholes residing in a galaxy. By this, we propose that these wormholes are mimickers of supermassive black holes residing at the galactic centers. In particular, we consider two wormhole spacetimes classes: the Damour-Solodukhin wormhole and the braneworld wormhole. While there is no classical matter model for the Damour-Solodukhin wormhole, the braneworld wormhole, on the other hand, is supported by a scalar-tensor theory on the four-dimensional brane. Intriguingly, it turns out that the presence of a dark matter halo surrounding these wormholes can tame the violations of energy conditions present in generic wormhole spacetimes. Our results also demonstrate that the galactic Damour-Solodukhin wormhole is more stable than its isolated counterpart under linear scalar perturbation, whereas we obtain the opposite behavior for the braneworld wormhole. The perturbation of these wormholes leads to echoes in the ringdown waveform, which are sensitive to the properties of the dark matter halo. To be precise, the time delay between two echoes is affected by the galactic matter environment, and it appears to be a generic effect present for any exotic compact object living in a galaxy. This allows us to identify the galactic parameters, independently from the gravitational wave measurements, if echoes are observed in future generations of gravitational wave detectors. For completeness, we have also analyzed the impact of the galactic environment on the photon sphere, the innermost stable circular orbits, and the shadow radius. It turns out that the dark matter halo indeed affects these locations, with implications for shadow and accretion physics.

DOI: [10.1103/PhysRevD.109.064043](https://doi.org/10.1103/PhysRevD.109.064043)**I. INTRODUCTION**

Understanding gravity at its extreme is the key to solving one of the most important problems of modern physics, i.e., constructing a self-consistent quantum theory of gravity [1–4]. The urge for quantizing gravity arises from the fact that, although it is well known how to quantize three of the four fundamental forces, namely, the strong, weak, and electromagnetic, and provide a unified description, so far gravity has remained elusive.¹ In the weak field regime, the gravitational interaction seems to be described extremely well by Einstein’s theory of general relativity [9–11], however, the dynamics of gravity in the strong field regime is currently being unwrapped [9]. Recent gravitational wave detections from the merger of binary black holes by the LIGO-VIRGO Collaboration [12–17] have

opened the window to probe the nature of gravity in the strong field regime, in particular, the physics near the horizon. Such an analysis is of utmost importance, given the fact that it is being hotly debated whether we really have a black hole or some ultracompact object, possibly involving quantum gravitational effects modifying the near horizon structure [18–22]. This leads to the exciting possibility of having horizonless but extremely compact objects mimicking the gravitational wave signals seen by the LIGO-VIRGO Collaboration [23–28].

Such ultracompact objects often have radii smaller than the Buchdahl radius [29–32], the limiting stellar configuration achieved using “normal” matter fields, and hence to model such compact objects we need exotic matter fields. Following this, such ultracompact objects are often referred to as exotic compact objects (ECOs). To model these ECOs one usually puts a partially reflecting surface slightly away from the location of the would-be horizon, such that the reflective surface is within the photon sphere, so they can mimic the ringdown waveform of a black hole [23–25,33,34]. However, due to the presence of a partially reflecting surface, the boundary condition near the would-be horizon changes—from being purely ingoing for the case of black holes to harboring both ingoing and outgoing modes, owing to the reflective nature of the surface [26,35]. These outgoing

*shauvikbiswas2014@gmail.com

†chiranjeeb.singha@saha.ac.in

‡tpsc@iacs.res.in

¹Here, by quantum gravity, we mean quantizing gravity with all of its nonlinear aspects included. In the linear regime, however, quantum gravity exists, which can be obtained from the fact that in the linear regime general relativity reduces to a massless spin-2 classical field theory on the flat background [5–7] and hence can be quantized using known prescriptions [8].

modes will lead to late-time echoes of the primary signal in the ringdown profile of gravitational waves. Despite having such an interesting structure, which can arise in various different contexts [27,36,37], there has been one major problem with these models—one puts forward such a reflective surface close to the horizon in an *ad hoc* manner—neither the reflectivity nor the location of the surface arises from some fundamental point of view. Subsequently, several attempts have been made to model the reflective surface appropriately, either by invoking quantum effects [21,22,38] or by considering wormhole geometries [33,39–42]. In both of these scenarios, the existence of such a partially reflective surface is a consequence and not an artifact. Wormholes, in particular, are spacetimes that connect two distinct universes via a throat [43,44], where these two universes can have their own photon sphere. So that, from the perspective of one universe, the angular momentum barrier associated with the photon sphere of the other universe acts as a partially reflecting surface [33,41]. Generic wormhole models have two major drawbacks: first of all, the formation channel of wormhole geometries is not known, and second, they violate the energy conditions. The second issue, namely, the violation of energy conditions, can be circumvented if we consider the braneworld scenario, where the matter field on the brane satisfies the energy conditions, but violations of energy conditions happen in bulk [41,45]. The final question regarding these wormhole geometries, and ECOs in general, is their stability. There have been several works discussing the stability of various ECOs [25,37,46–48], including wormhole geometries [41,49–53], albeit in the isolated scenario. Also, several works have been done to develop astrophysical techniques [54–58] to detect wormholes in the extended theories of gravity.

However, there are no isolated objects in our Universe. As is well known from various experiments—from the flatness of the rotation curves of galaxies [59–62], the dynamics of hot gas in clusters [63], and gravitational lensing experiments [64], among others—95% mass of the Galaxy comes from that of nonbaryonic matter, namely, the dark matter [65,66]. Therefore, any compact object, be it a black hole or an ECO, must reside in an environment involving dark matter, and hence the spacetime geometry must be affected by the same. Recently, a fully relativistic analysis was presented in [67], where the spherically symmetric metric of a black hole spacetime was derived in the presence of a galactic matter distribution following the Hernquist-type density profile [68],²

$$\rho(r) = \frac{Ma}{2\pi r(r+a)^3}, \quad (1)$$

where M is the mass of the dark matter halo and a is a typical length scale associated with the dark matter

²For galactic black hole solutions with other mass profiles, see [69].

distribution in the galaxy. Motivated by the above density profile, the mass profile of a galactic black hole becomes

$$m(r) = M_{\text{BH}} + \frac{Mr^2}{(r+a)^2} \left(1 - \frac{2M_{\text{BH}}}{r}\right)^2, \quad (2)$$

where M_{BH} is the mass of the central black hole. The geometry resulting from the above mass profile is reminiscent of the Einstein cluster [70]. Note that the above mass profile keeps the existence of the black hole horizon intact, even in the presence of a galaxy. It is worthwhile to mention that galactic matter also provides an effective shielding mechanism when the central black hole is electrically charged [71]. Motivated by the fully relativistic analysis involving galactic black holes, in this paper, we consider the case of a wormhole in the Galaxy. Just as galactic black holes keep their horizons intact, we will depict appropriate mass profiles that keep the location of the throat of the galactic wormhole unchanged. We start by considering the environmental effects on the Damour-Solodukhin wormhole and then proceed toward discussing the braneworld wormhole in a galaxy.

In the case of braneworld wormholes, one can have two possible of situations—(i) wormholes in the Randall-Sundrum (RS)1 scenario, involving compact extra dimension and (ii) wormholes in the RS2 scenario, with non-compact extra dimension. The former case is described by two branes, such that all the standard model particles are localized on the visible brane, while for gravity the effective Einstein equation takes the form of a scalar-tensor theory of gravity, where the scalar field originates from the interbrane separation [72]. Therefore, in this case, the scalar field captures any nonlocal bulk effect. On the other hand, in the latter case, the effective Einstein equation on a vacuum brane inherits an extra contribution from the electric part of the projected bulk Weyl tensor, capturing the nonlocal bulk effects on the brane. In both the cases discussed above, the field equations are not closed in the sense that the solutions of the effective Einstein equation itself either need knowledge of the bulk Weyl tensor or the evolution of the scalar field. In addition to the wormhole geometry in the RS1 model considered here, there are several other wormhole solutions to the gravitational field equations in the context of the RS2 scenario as well, with similar as well as distinct solutions [52,73–75]. It will be worth pursuing the stability of these solutions in the RS2 scenario and subsequently embedding them in a dark matter halo.

Here, we wish to address the question of how the presence of a dark matter halo can cure the violation of energy conditions, which were present for the isolated wormhole geometry. Moreover, we will also study the scalar perturbation of galactic wormhole geometries and shall describe the distinguishing features in the ringdown signal of a galactic wormhole in contrast to that of an isolated wormhole spacetime. We also analyze how environmental effects

can influence the location of the photon sphere, the innermost stable circular orbit (ISCO), and finally the shadow radius.

This paper is organized as follows: In Sec. II we will discuss the basic strategy to model wormholes involving environmental effects due to the surrounding dark matter halo. Following this, in Sec. II A we will model a galactic Damour-Solodukhin wormhole, while Sec. II B will be dedicated to the analysis of the braneworld wormhole. Subsequently, having laid down the geometry of the braneworld wormhole spacetime, in Sec. III we will study the massless scalar perturbation and shall determine the effective potential experienced by it. Finally, using the transfer matrix method [49], we will find the scalar quasinormal modes and shall also solve the master equation in the time domain in order to obtain the ringdown waveform. We conclude in Sec. IV with a discussion of our results and provide some future prospects.

In our calculations we will set $c = 1 = G$. The lowercase Greek indices μ, ν, \dots will denote the four-dimensional spacetime coordinates. We will follow the mostly positive signature convention for our metric, such that the Minkowski metric in four spacetime dimensions takes the form $\eta_{\mu\nu} = \text{diag.}(-1, +1, +1, +1)$.

II. GEOMETRY OF WORMHOLES AT THE CENTER OF GALAXIES

In this section, we present the static and spherically symmetric wormhole geometries with a spherical galactic halo surrounding them. By and large, the analysis parallels the case of a galactic black hole, but differs in the details and also in the interpretation. Moreover, in the present context, we solve the following Einstein equations:

$$G_{\mu\nu} = T_{\mu\nu}^{(g)} + T_{\mu\nu}^{(w)}, \quad (3)$$

where, $T_{\mu\nu}^{(g)}$ is the energy-momentum tensor for the galactic matter and $T_{\mu\nu}^{(w)}$ is the energy-momentum tensor supporting the wormhole geometry, often violating the energy conditions. The galactic matter is considered to be distributed spherically around the central wormhole, such that the (wormhole + dark matter halo) can be considered as a static and spherically symmetric configuration together. Moreover, the configuration is supposed to be static, i.e., no radial outflow should be present. Thus, as in the black hole case, here also we let

$$T_{\nu}^{\mu(g)} = \text{diag}\left(-\rho^{(g)}, 0, p_{\perp}^{(g)}, p_{\perp}^{(g)}\right), \quad (4)$$

where $\rho^{(g)}$ is the density of the dark matter halo surrounding the central wormhole and $p_{\perp}^{(g)}$ is the transverse pressure, perpendicular to the radial direction, acting on the dark matter particles.

The energy-momentum tensor $T_{\mu\nu}^{(w)}$ supporting the wormhole depends on the details of the wormhole geometry and differs from one wormhole solution to another. In what follows, we will discuss the structure of $T_{\mu\nu}^{(w)}$ for two cases: (a) the Damour-Solodukhin wormhole and (b) the braneworld wormhole. In the case of the Damour-Solodukhin wormhole, $T_{\mu\nu}^{(w)}$ does not arise from some well-defined matter model and is of phenomenological origin, while for braneworld wormhole, $T_{\mu\nu}^{(w)}$ depends on the length of the higher dimension and hence has a well-motivated matter model. We will provide explicit expressions for these quantities shortly, which will be useful in constructing the solution of galactic wormholes with an appropriate dark matter profile.

Since the total configuration involving a wormhole and the galactic matter is spherically symmetric and stationary, for this system, we may consider the following static and spherically symmetric metric ansatz:

$$ds^2 = -f(r)dt^2 + \left(1 - \frac{2m(r)}{r}\right)^{-1} dr^2 + r^2 d\Omega_2^2, \quad (5)$$

for describing the geometry of a galactic wormhole. The system has four unknown functions, the mass profile $m(r)$, the g_{tt} component $f(r)$, the energy density $\rho^{(g)}$, and the transverse pressure $p_{\perp}^{(g)}$. Whereas there are three independent equations relating them—these are the G_t^t and G_r^r components of Einstein's equations and the conservation equation $\nabla_{\mu} T_{\nu}^{\mu(g)} = 0$. Note that, by construction, the energy-momentum tensor supporting the wormhole is conserved, i.e., $\nabla_{\mu} T_{\nu}^{\mu(w)} = 0$. Thus, the system of equations does not close, and hence some additional input is necessary. In the case of black holes, fixing the mass function provides the necessary condition to close the system of equations, which we also follow in the present context involving wormholes.

The choice of the mass function is constrained from several directions. First of all, we need to choose the mass profile $m(r)$ such that, at a large distance from the wormhole throat, it should reproduce the Hernquist-type density profile. While at a small distance, comparable to the wormhole throat, the mass function should resemble that of the wormhole. Having specified the mass profile, one can solve the G_r^r component of Einstein's equation, as in Eq. (3), to determine the other metric component g_{tt} . Finally, the conservation law for the galactic energy-momentum tensor provides the transverse pressure, and the G_t^t component of Einstein's equations provides the energy density of the dark matter halo. Note that a traversable wormhole requires violation of the null and the weak energy conditions near the throat [43], since the wormhole throat acts as a geodesic-defocusing lens. This is achieved by the energy-momentum tensor $T_{\nu}^{\mu(w)}$ in Eq. (3),

which violates these energy conditions. The above summarizes the basic strategy to solve for the geometry of the galactic wormhole, which we will adopt in the subsequent sections in determining the environmental effect of a galaxy on Damour-Solodukhin and braneworld wormholes.

A. Damour-Solodukhin wormhole in a galaxy

In this section, we provide the environmental effects of galactic dark matter on the Damour-Solodukhin wormhole. For this purpose, we briefly review the isolated Damour-Solodukhin wormhole spacetime, which is described by the following line element [76]:

$$ds^2 = -\left(1 - \frac{2M_1}{r}\right)dt^2 + \left(1 - \frac{2M_2}{r}\right)^{-1}dr^2 + r^2d\Omega_2^2, \quad (6)$$

$$M_2 = M_1(1 + \lambda^2).$$

As evident from the above line element, it follows that $r = 2M_2$ is a null hypersurface, but it is not a horizon because the norm of the timelike Killing vector field $(\partial/\partial t)$ is given by g_{tt} , which does not vanish at $r = 2M_2$. Therefore, timelike observers can remain at rest on that hypersurface, and hence $r = 2M_2$ is not a Killing horizon, but rather the throat of the wormhole. Moreover, calculation of the Kretschmann scalar $K \equiv R_{\mu\nu\alpha\beta}R^{\mu\nu\alpha\beta}$ shows that $K \propto r^{-6}(r - 2M_1)^{-4}$, which is finite at $r = 2M_2$, but diverges at $r = 2M_1$. Therefore, if one wants to continue the spacetime through the null hypersurface at $r = 2M_2$, it will have a naked singularity at $r = 2M_1$, which will violate the weak version of the cosmic censorship conjecture. In order to avoid this pathology, one truncates the spacetime at $r = 2M_2$ and considers two copies of the spacetime glued at this radius. The resulting spacetime corresponds to the Damour Solodukhin wormhole with a null throat at $r = 2M_2$.

The above metric is a solution of Einstein's equations, provided the right-hand side of Einstein's equations involves an energy-momentum tensor with an anisotropic fluid, which has the following components:

$$T_v^{u(w)} = \text{diag}\left(0, p_r^{(ds)}, p_\perp^{(ds)}, p_\perp^{(ds)}\right);$$

$$p_r^{(ds)} = -\frac{\lambda^2 M_1}{4\pi r^2 (r - 2M_1)}, \quad p_\perp^{(ds)} = \frac{(r - M_1)\lambda^2 M_1}{8\pi r^2 (r - 2M_1)^2}. \quad (7)$$

As evident from the above energy-momentum tensor, the energy density $\rho^{(ds)}$ supporting the wormhole identically vanishes, while the radial pressure $p_r^{(ds)}$ is nonzero but negative. Thus, it follows that the wormhole spacetime violates both the null and weak energy conditions, as $\rho^{(ds)} + p_r^{(ds)} < 0$, while $\rho^{(ds)} + p_\perp^{(ds)} > 0$. Thus, we have described the geometry and the source of the isolated Damour-Solodukhin wormhole, which will be used

to construct a galactic wormhole with the Damour-Solodukhin wormhole at the center.

1. Geometry of the galactic Damour-Solodukhin wormhole

As already emphasized above, the first step in determining the environmental effect on the Damour-Solodukhin wormhole is to provide a suitable mass function with desired properties. Motivated by the corresponding mass profile for galactic black holes, here we consider the following mass profile (for an alternative mass profile, see Appendix A):

$$m(r) = M_2 + \frac{Mr^2}{(r+a)^2} \left(1 - \frac{2M_1}{r}\right) \left(1 - \frac{2M_2}{r}\right). \quad (8)$$

Here, M is the mass, and a is the characteristic radius of the dark matter halo. Moreover, there are three cases to consider—(a) for $r \ll a$, the mass function simply becomes $m(r) \approx M_2$, i.e., at radii much smaller compared to the galactic scale a , the geometry is that of an isolated Damour-Solodukhin wormhole with mass M_2 ; (b) for $r \gg M_2$, the above mass profile reduces to $M_2 + \{Mr^2/(r+a)^2\}$, i.e., the metric is governed by the mass profile of the galactic halo; and finally (c) for $r \gg a$, we obtain for the mass profile $(M_2 + M)$, which corresponds to the Arnowitt-Deser-Misner (ADM) mass of the galactic wormhole spacetime. For the above mass function, the g^{rr} component of the metric describing the galactic wormhole becomes

$$g^{rr} = \left(1 - \frac{2M_2}{r}\right) \left[1 - \frac{Mr}{(r+a)^2} \left(1 - \frac{2M_1}{r}\right)\right]. \quad (9)$$

Therefore, $r = 2M_2$ is still a null hypersurface, and as we will demonstrate later, it also corresponds to the throat of the wormhole. Given the mass profile and the g^{rr} component of the metric, the G^t_t component of Einstein's equations yields $m'(r) = 4\pi r^2(\rho_{(ds)}^{(g)} + \rho^{(ds)})$. Since the energy density of matter $\rho^{(ds)}$, supporting the Damour-Solodukhin wormhole, identically vanishes, for the mass profile in Eq. (8), we obtain the following density profile for the galactic dark matter distribution:

$$\rho_{(ds)}^{(g)} = \frac{2M(1 - \frac{2M_1}{r})(a + 2M_1)}{4\pi r(a+r)^3} + \lambda^2 \frac{M[M_1(r - 4M_1) - aM_1]}{2\pi r^2(a+r)^3}. \quad (10)$$

Note that the above energy density is non-negative for $r \geq 2M_2$. Additionally, for $M \rightarrow 0$, the energy density identically vanishes, since it is created by the galactic matter alone. Similarly, for $r \sim 2M_2 \ll a$, it follows that $\rho_{(ds)}^{(g)} \sim (1/a^2)$ and vanishes as a becomes large. This is also consistent with the result that the above density is created

by the galactic dark matter distribution alone and has no contribution from the energy-momentum tensor for the wormhole. Finally, for $r \gg 2M_2$ and for $\lambda \ll 1$, the above density profile reduces to the Hernquist profile, described by Eq. (1), as expected. Similarly, one can compute the tangential pressure by solving the G^θ_θ component of Einstein's equation or imposing the conservation of energy. The exact expression of the tangential pressure ($p_\perp^{(g)}$ ($p_\perp^{(ds)}$)) is given in Appendix B.

The determination of the g_{tt} component of the metric is achieved by solving the G^r_r component of Einstein's equation, which reads

$$\begin{aligned} \frac{1}{r} \left(1 - \frac{2m(r)}{r} \right) \frac{d \ln f}{dr} - \frac{1}{r^2} + \frac{1}{r^2} \left(1 - \frac{2m(r)}{r} \right) \\ = 8\pi \left(p_r^{(g)} + p_r^{(ds)} \right). \end{aligned} \quad (11)$$

For the galactic matter distribution, there are no radial out-/inflows present, and hence we must have $p_r^{(g)} = 0$. However, unlike the case of black holes, matter distribution supporting wormholes has nonzero radial pressure, which for the Damour-Solodukhin wormhole is given by Eq. (7). For the above radial pressure and the mass profile given by Eq. (8), we find

$$\begin{aligned} f(r) &= \left(1 - \frac{2M_1}{r} \right) e^\gamma, \\ \gamma &\equiv -\pi \sqrt{\frac{M}{\xi}} + 2\sqrt{\frac{M}{\xi}} \tan^{-1} \left(\frac{r + a - M}{\sqrt{M\xi}} \right), \end{aligned} \quad (12)$$

where $\xi \equiv 2a - M + 4M_1$. It is clear that, like the g^{rr} component, $f(r \rightarrow \infty) \rightarrow 1$ and hence the geometry is asymptotically flat. Interestingly, for the above mass profile, the g_{tt} component is independent of M_2 and appears

in the same form as the galaxy with a central black hole [67], provided we make the replacement $M_1 \rightarrow M_{\text{BH}}$. Note that the surface $r = 2M_1$ is where the norm of the timelike Killing vector field ($\partial/\partial t$) vanishes, but is not null. Thus, the above spacetime, described by the metric elements presented in Eqs. (9) and (12) depicts a wormhole geometry with its throat located at $r = 2M_2$, but incorporates the effect of the dark matter halo surrounding the same. We will refer to this geometry as the galactic Damour-Solodukhin wormhole.

Let us now explore the status of the energy conditions for the galactic Damour-Solodukhin wormhole, in particular, it follows that total matter-energy density supporting this wormhole is simply given by $\rho_{(ds)}^{(g)}$, which is positive for $r > 2M_2$, and hence the weak energy condition is satisfied everywhere outside the wormhole. To see what happens for the null energy condition, we have plotted the sum of total energy density and radial pressure against the radial coordinate r in Fig. 1. As evident, the energy density comes from the galactic dark matter, while the radial pressure arises from the matter supporting the wormhole, such that $\rho + p_r \equiv \rho_{(ds)}^{(g)} + p_r^{(ds)}$, among which the contribution by the energy density is positive, while the radial pressure contributes negatively. As a consequence, and as clear from Fig. 1, the violation of the null energy condition for the galactic Damour-Solodukhin wormhole happens for a much smaller spatial region ($2M_2 \leq r < r_0$), compared to the Damour-Solodukhin wormhole, where the violation is present throughout the space ($2M_2 \leq r < \infty$). The radius r_0 , below which the violation of the null energy condition happens, can be obtained by solving the algebraic equation $\rho + p_r = 0$, which yields

$$r_0 \simeq 2M_2 + a \sqrt{\frac{M_2}{2M}} \lambda, \quad (13)$$

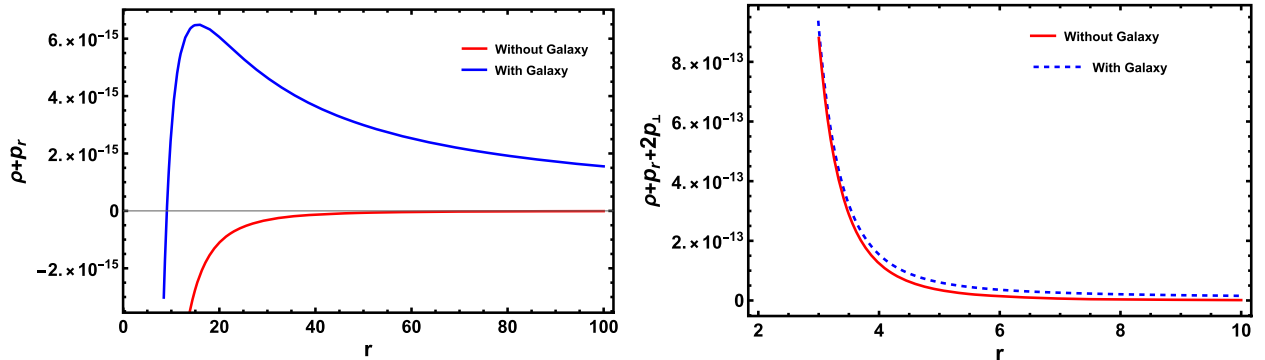


FIG. 1. The quantity $(\rho + p_r)$ has been depicted on the left as a function of the radial coordinate r for two cases—(a) without the dark matter halo and (b) with a dark matter halo, with the following choices of the parameters: $(a/M_1) = 10^8$, $(M/M_1) = 10^4$, and $\lambda = 10^{-5}$. This plot clearly demonstrates that the null energy condition is violated everywhere in the absence of a dark matter halo. However, in the presence of a galaxy, i.e., when the wormhole is surrounded by a dark matter halo, the null energy condition is violated in a small radial interval, close to the throat. On the other hand, the right plane plot presents the variation of $\rho + p_r + 2p_\perp$ with the radial coordinate. As evident, this quantity is indeed positive with or without the galaxy.

definitely greater than the throat location of the wormhole. Thus, it is appropriate to argue that, in the presence of a galactic halo, the violation of the null energy condition can be tamed, such that for all space outside the radial coordinate r_0 the null energy condition is satisfied.³

2. Properties of the galactic Damour-Solodukhin wormhole

At this stage, it will be instructive to specify the hierarchy between various mass scales and λ . To mimic galactic observations, we assume that $a > M \gg M_1$ [77] and restrict the parameter λ , such that $\lambda \ll 1$. The first assumption simply states that the size of the galactic dark matter distribution is much larger than the size of the wormhole. This is typical of any astrophysical scenario, where the size of the central compact object is several orders of magnitude smaller than the size of the galaxy. The second assumption makes the underlying wormhole spacetime, described by Eq. (6), close to that of a Schwarzschild black hole mimicker. Using these assumptions, we can expand the relevant expressions in the powers of λ and the dimensionless ratio (M_1/a) . Such expansion enables us to determine the closed-form expressions for various quantities associated with the galactic Damour-Solodukhin wormhole, e.g., the radius of the photon sphere and the ISCO.

In what follows, we will provide a brief derivation of the equation governing the location of the photon sphere. Since photons move along null geodesics, we can take l^μ to be the tangent along the null geodesics, satisfying $l^\mu l_\mu = 0$. Because of the Killing symmetries of the spacetime, we have conserved energy $E = -l_\mu(\partial/\partial t)^\mu$ and conserved angular momentum $L = l_\mu(\partial/\partial\phi)^\mu$. The condition $l^\mu l_\mu = 0$ yields the following equation for the radial component of the null geodesic:

$$g_{rr}(l^r)^2 - \frac{L^2}{r^2} = -g^{tt} \frac{L^2}{b^2}, \quad (14)$$

where the impact parameter is defined as $b = (L/E)$. It is evident from Eq. (14) that the potential experienced by any null geodesics, including photon, is $V_{\text{ph}} = -(L^2/r^2)g_{tt}$. Using the conditions of having a circular photon orbit—(a) $V_{\text{ph}} = 0$ and (b) $V'_{\text{ph}} = 0$, leads to the condition $rg'_{tt}(r) = 2g_{tt}$ at $r = r_{\text{ph}}$. Solving this algebraic equation in the present context yields the following equation for the photon sphere, to leading order in (M_1/a) :

³One can also show that $\rho + p_\perp$ is positive, as well as $\rho + p_r + 2p_\perp > 0$, for $r \geq 2M_2$. Thus, the strong energy condition is also satisfied everywhere in the galactic Damour-Solodukhin wormhole for $r \geq r_0$.

$$r_{\text{ph}} = 3M_1 \left(1 + \frac{MM_1}{a^2} \right). \quad (15)$$

It is to be emphasized that the photon sphere as obtained above is a special case of the photon region [78–83], which is defined as a compact region of the spacetime where photons can travel endlessly without going to infinity or to the event horizon.

Note that, in the limit of $M \rightarrow 0$, from Eq. (15) we get back the result for the photon sphere of the isolated Damour-Solodukhin wormhole, as we should. Also, the presence of a dark matter halo increases the radial location of the photon sphere, compared to the case of an isolated wormhole. The computation of the ISCO radius follows from the effective potential experienced by a massive particle moving in this spacetime; in particular, one simultaneously imposes three conditions: $V_{\text{eff}} = 0$, $V'_{\text{eff}} = 0$, and $V''_{\text{eff}} = 0$, which provides an algebraic equation for the radial coordinate with the following solution:

$$r_{\text{ISCO}} = 6M_1 \left(1 - \frac{32MM_1}{a^2} \right). \quad (16)$$

Here also, in the limit of $M \rightarrow 0$, we get back the ISCO radius associated with an isolated Damour-Solodukhin wormhole; however, in contrast to the photon sphere, the radial location of the ISCO for the galactic Damour-Solodukhin wormhole decreases compared to the isolated Damour-Solodukhin wormhole. Along similar lines, one can compute the shadow radius associated with the galactic Damour-Solodukhin wormhole, which is given by

$$r_{\text{sh}} = 3\sqrt{3}M_1 \left[1 + \frac{M}{a} + \frac{M(5M - 18M_1)}{6a^2} \right]. \quad (17)$$

As for the case of the photon sphere, the shadow radius also reduces to the desired expression $3\sqrt{3}M_1$ in the absence of galactic matter, i.e., in the limit $M \rightarrow 0$, and increases in the presence of galactic matter (as $M \gg M_1$). This suggests that the shadow radius of any compact object in a galactic environment will be larger compared to the isolated object. It is worth pointing out that all the quantities derived above, namely, the photon sphere r_{ph} , the ISCO radius r_{ISCO} , and the shadow radius r_{sh} depend on the g_{tt} component and its derivatives alone, and hence these are all independent of the wormhole parameter λ . Both the photon sphere and the shadow radii are plotted in Fig. 2, against the dimensionless galactic scale (M/a) . The figure explicitly demonstrates how the photon sphere and the shadow radius are affected by the presence of a galaxy; in particular, it follows that the presence of dark matter halo increases the radii compared to the isolated wormhole counterpart.

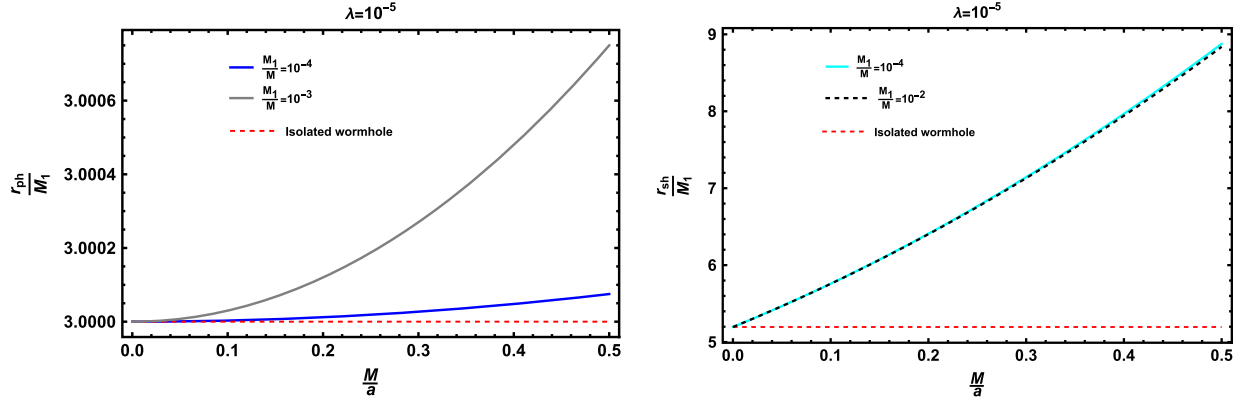


FIG. 2. The radial location of the photon sphere r_{ph} as a function of the compactness of the galaxy (M/a) has been presented on the left. The plot shows that, in the presence of a galaxy, the radial location of the photon sphere increases compared to that of the isolated Damour-Solodukhin wormhole. On the other hand, the right panel demonstrates the variation of the shadow radius r_{sh} of the galactic Damour-Solodukhin wormhole as a function of the galactic compactness (M/a) and depicts a similar behavior. All the radii are scaled by the ADM mass of the wormhole M_1 .

B. Galactic wormhole in the braneworld scenario

We start by briefly summarizing the isolated braneworld wormhole scenario. In this case, one assumes that we live in a four-dimensional hypersurface, known as the brane, embedded in a five-dimensional spacetime, referred to as the bulk. The bulk spacetime is generically taken to be endowed with a negative cosmological constant, while the extra spacelike extra dimension (denoted as y) is taken to be compact. We consider a two-brane system, where the Planck brane is located at $y = 0$ (typical energy scale in this brane is Planckian order) and the visible brane is located at $y = \ell$ (energy scale in this brane is a few tens of TeV). The metric in the bulk spacetime can be expressed as [72]

$$ds^2 = e^{2\phi(x)} dy^2 + \tilde{g}_{\mu\nu}(y, x) dx^\mu dx^\nu, \quad (18)$$

where $\phi(x)$ is called the radion field and is related to the separation between the two branes, such that the proper distance between the two branes is given by $d(x) = e^{\phi(x)} \ell$. It is expected that the curvature length scale of the bulk spacetime, which is given by ℓ , will be much smaller compared to the corresponding length scale on the brane. This is because the curvature of the bulk spacetime is much larger than the curvature on the brane, and hence an inverse relationship exists between the respective length scales. Thus, we can expand the gravitational field equations as a power series in $(\ell/\text{brane curvature scale})$. This leads to the following effective Einstein equation on the visible brane [72]:

$$G_{\mu\nu} = \frac{\kappa^2}{\ell\Phi} T_{\mu\nu}^{(\text{vis})} + \frac{\kappa^2(1+\Phi)}{\ell\Phi} T_{\mu\nu}^{(\text{Pl})} + \frac{1}{\Phi} T_{\mu\nu}^\Phi; \quad (19)$$

$$\Phi = \exp[2e^{\phi(x)}] - 1,$$

where

$$T_{\mu\nu}^\Phi = \left(\nabla_\mu \nabla_\nu \Phi - g_{\mu\nu} \nabla^\alpha \nabla_\alpha \Phi \right) - \frac{3}{2(1+\Phi)} \left(\nabla_\mu \Phi \nabla_\nu \Phi - \frac{1}{2} g_{\mu\nu} \nabla_\alpha \Phi \nabla^\alpha \Phi \right). \quad (20)$$

In the above expression for the effective gravitational field equations on the visible brane, presented in Eq. (19), except for the energy-momentum tensor $T_{\mu\nu}^\Phi$, arising from the radion field, we have two additional contributions— $T_{\mu\nu}^{(\text{vis})}$ and $T_{\mu\nu}^{(\text{Pl})}$, which are the energy-momentum tensors of the matter fields trapped on the visible brane and the Planck brane, respectively. Moreover, the ratio (κ^2/ℓ) acts as an effective gravitational constant on the brane, where κ^2 is the bulk gravitational constant. Note that the metric $g_{\mu\nu}$ on the visible brane is related to the metric $\tilde{g}_{\mu\nu}$, appearing in Eq. (18), by a conformal factor $\exp(-d/\ell)$. In addition to the gravitational field equations on the brane, we also obtain a field equation for the radion field Φ , which reads [72]

$$\nabla^\alpha \nabla_\alpha \Phi = \frac{\kappa^2 T^{(\text{Pl})} + T^{(\text{vis})}}{\ell} - \frac{1}{2\omega + 3} \frac{d\omega}{d\Phi} (\nabla^\alpha \Phi)(\nabla_\alpha \Phi) \quad (21)$$

$$\text{with } \omega = -\frac{3\Phi}{2(1+\Phi)},$$

where $T^{(\text{vis})}$ and $T^{(\text{Pl})}$ are, respectively, the traces of the matter energy-momentum tensor of the visible and the Planck brane. In what follows, we will consider the case of a vacuum Planck brane, i.e., we will assume $T_{\mu\nu}^{(\text{Pl})} = 0$. Note that the Bianchi identity when applied to Eq. (19) must imply the field equation for the radion field for consistency, which we have reproduced in Appendix C. Given the

gravitational field equations on the brane and the radion field equations presented above, in the context of static and spherically symmetry, the following solution can be obtained (for details, see [45]):

$$ds^2 = -\frac{1}{(\chi+1)^2} \left(\chi + \sqrt{1 - \frac{2M_1}{r}} \right)^2 dt^2 + \left(1 - \frac{2M_1}{r} \right)^{-1} dr^2 + r^2 d\Omega_2^2, \quad (22)$$

with the radial dependence of the radion incarnation Φ on the visible brane being

$$\Phi(r) = \frac{\Phi_1^2}{4} \left[\ln \left(\chi + \sqrt{1 - \frac{2M_1}{r}} \right) \right]^2 + \Phi_1 \sqrt{\Phi_0 + 1} \ln \left(\chi + \sqrt{1 - \frac{2M_1}{r}} \right) + \Phi_0, \quad (23)$$

where Φ_1 and Φ_0 are some constants and chosen in such a way that the two branes never collide [41]. Note that the field equation for Φ admits two solutions: the above solution is valid for $\chi \neq 0$, while for $\chi = 0$, we have $\Phi = \text{constant}$. Therefore, nonzero values of the parameter χ yield a nontrivial scalar field configuration and also a distinct static and spherically symmetric geometry. For $\chi = 0$, we get back the Schwarzschild solution with a constant radion field Φ , as expected. The above solution for the field Φ can also be expressed in terms of isotropic coordinate r' , related to the radial coordinate r by the following relation: $r = r' \{1 + (M_1/2r')\}^2$, such that Eq. (23) reduces to the corresponding expression presented in [45]. For our purpose, the solution for Φ in terms of the radial coordinate r will be sufficient.

The above solution for the metric $g_{\mu\nu}$ and the field Φ arises based on the assumption that the Ricci scalar of the visible brane vanishes and the brane matter is an anisotropic fluid, described by the following energy-momentum tensor: $T_{\nu}^{\mu(\text{vis})} = \text{diag}(-\rho^{(\text{vis})}, p_r^{(\text{vis})}, p_{\perp}^{(\text{vis})}, p_{\perp}^{(\text{vis})})$ such that its trace vanishes [75,84,85]. However, what enters into the gravitational field equations is a combination of the brane energy-momentum tensor $T_{\mu\nu}^{(\text{vis})}$ and the radion field energy-momentum tensor $T_{\mu\nu}^{\Phi}$. Thus, in our subsequent calculations, we will only need the expressions for the components of the total energy-momentum tensor, which reads

$$\begin{aligned} T_{\nu}^{\mu(b)} &\equiv \frac{1}{\Phi} T_{\nu}^{\mu(\text{vis})} + \frac{\ell}{\kappa^2 \Phi} T_{\nu}^{\mu\Phi} = \text{diag} (0, p_r^{(b)}, p_{\perp}^{(b)}, p_{\perp}^{(b)}); \\ p_r^{(b)} &= -\frac{\chi M_1}{8\pi r^3 \left(\chi + \sqrt{1 - \frac{2M_1}{r}} \right)}, \\ p_{\perp}^{(b)} &= \frac{2\chi M_1}{8\pi r^3 \left(\chi + \sqrt{1 - \frac{2M_1}{r}} \right)}. \end{aligned} \quad (24)$$

Note that, for $\chi = 0$, the line element in Eq. (22) reduces to that of Schwarzschild spacetime and Φ becomes constant and, therefore, nondynamical. For $\chi > 0$, Eq. (22) represents a wormhole solution with a null throat at $r = 2M_1$ because at this radius the metric component g^{rr} vanishes, but the timelike Killing vector field $(\partial/\partial t)^\mu$ remains timelike. Thus, the surface $r = 2M_1$ is not a Killing horizon; hence, the above spacetime does not describe a black hole geometry. On the other hand, the spacetime becomes complex beyond $r = 2M_1$, thanks to the presence of the square root term, and hence is not extendable beyond this radius. Thus, one joins two copies of the spacetime at $r = 2M_1$, akin to wormhole geometries, and this radius is referred to as the throat of the wormhole. Therefore, Eq. (22) describes a wormhole geometry, mimicking the Schwarzschild spacetime for small wormhole parameter χ and large r , with $\chi \gtrsim 0$. Moreover, the total energy-momentum tensor $T_{\mu\nu}^{(b)}$ violates the weak as well as the null energy conditions everywhere, as $\rho^{(b)} + p_r^{(b)} < 0$, which is another characteristic feature of wormhole geometries.

1. Geometry of the galactic braneworld wormhole

Having outlined the geometry and the associated gravitational field equations of an isolated wormhole spacetime on the brane, we now incorporate environmental effects due to the surrounding dark matter halo. The geometry is taken to be static and spherically symmetric, such that the line element of the galactic braneworld wormhole is still given by Eq. (5). However, the method adopted in the context of the Damour-Solodukhin wormhole does not apply here due to the nonpolynomial nature of the background metric describing the braneworld wormhole, in particular, the square root term in the g_{tt} component of the metric. Also, Einstein's equations in the presence of galactic matter on the brane become

$$G_{\mu\nu} = \frac{\kappa^2}{\ell} \left(\frac{1}{\Phi} T_{\mu\nu}^{(g)} + T_{\mu\nu}^{(b)} \right), \quad (25)$$

where $T_{\mu\nu}^{(b)}$ contains the contribution from the scalar and the matter on the visible brane, which for the isolated wormhole case has already been presented in Eq. (24) and the energy-momentum tensor of the galactic matter is taken to be $T_{\nu}^{\mu(g)} = \text{diag}(-\rho^{(g)}, 0, p_{\perp}^{(g)}, p_{\perp}^{(g)})$. Since we have modeled the galaxy using an anisotropic fluid with vanishing radial pressure, in the presence of the galaxy we have five unknowns: (i) $\rho^{(g)}$, (ii) $p_{\perp}^{(g)}$, (iii) g_{tt} , (iv) g_{rr} , and (v) Φ . On the other hand, we have three equations at our disposal, namely, (a) two Einstein equations corresponding to G^r_r and G^t_t components and (b) the field equation for the radion incarnation Φ . Note that the conservation of the energy-momentum tensor follows from the above three equations. Therefore, to close the system of differential equations and in order to determine the radial dependence

of the field Φ , we fix the metric component g_{tt} and the mass profile $m(r)$ such that

$$f(r) = \frac{1}{(\chi + 1)^2} \left(\chi + \sqrt{1 - \frac{2M_1}{r}} \right)^2 e^{\gamma};$$

$$\gamma = -\pi \sqrt{\frac{M}{\xi}} + 2 \sqrt{\frac{M}{\xi}} \tan^{-1} \left[\frac{r + a - M}{\sqrt{M\xi}} \right], \quad (26)$$

$$m(r) = M_1 + \frac{Mr^2}{(r+a)^2} \left(1 - \frac{2M_1}{r} \right)^2, \quad (27)$$

with $\xi = 2a - M + 4M_1$. Here M is the mass of the dark matter halo, and a is a typical galactic length scale. The above choice is motivated by several results: (a) In the limit $\chi \rightarrow 0$, the above expression for g_{tt} reduces to the solution for a galactic black hole, presented in [67], as it should; (b) in the limit $M \rightarrow 0$, the function $f(r)$ reduces to the corresponding metric component of the isolated braneworld wormhole; and (c) the Killing vector $(\partial/\partial t)$ remained timelike at $r = 2M_1$, typical of a wormhole spacetime. Along identical lines, it also follows that the mass profile has all the desired properties as described above, and in addition, we have (a) the surface $r = 2M_1$ is a null hypersurface, since g^{rr} vanishes there, and (b) for $r \gg 2M_1$, the above mass profile reduces to the Hernquist profile. Therefore, the above is also a viable mass profile for the braneworld wormhole embedded in a dark matter halo.

Using these metric components, we can calculate the Ricci scalar associated with the galactic braneworld wormhole, while keeping terms up to $\mathcal{O}(1/a^2)$, which reads

$$R = \frac{2M(12M_1^2 - 10M_1r + 2r^2)}{a^2r^2(r - 2M_1)}. \quad (28)$$

As expected, the Ricci scalar R vanishes for $M \rightarrow 0$, i.e., for the isolated wormhole. In particular, taking the trace of Eq. (25) and using the result that $T^{\mu(\text{vis})}_{\mu} = 0$, as well as the equation of motion of the radion incarnation field Φ ,

$$\nabla^\alpha \nabla_\alpha \Phi - \frac{1}{2(1+\Phi)} \nabla^\alpha \Phi \nabla_\alpha \Phi = \frac{\kappa^2 (1+\Phi) T^{(g)}}{\ell^3}, \quad (29)$$

it follows that

$$R = -\frac{\kappa^2}{\ell} T^{(g)}. \quad (30)$$

This result shows that the Ricci scalar for the galactic braneworld wormhole only depends on the trace of the galactic matter. Further, using Eq. (28) we can write the above expression as

$$\rho^{(g)} - 2p_{\perp}^{(g)} = \frac{\ell}{\kappa^2} \frac{2M(12M_1^2 - 10M_1r + 2r^2)}{a^2r^2(r - 2M_1)}. \quad (31)$$

To determine the explicit form of $p_{\perp}^{(g)}$ and $\rho^{(g)}$, one needs to know the solution for the field Φ , which can be obtained by solving Eq. (29). However, the nonpolynomial nature of the metric components poses a serious problem for obtaining the most general analytic solution of Φ . Thus, we assume that Φ depends on only the radial coordinate and hence express the field equation, namely, Eq. (29), in the following form:

$$\frac{d^2\epsilon}{dr^2} + \frac{d}{dr} \left[\ln r^2 \sqrt{f(r) \left(1 - \frac{2m(r)}{r} \right)} \right] \frac{d\epsilon}{dr} = -\frac{\epsilon}{6} R \left(1 - \frac{2m(r)}{r} \right),$$

$$\Phi(r) \equiv \epsilon^2(r) - 1. \quad (32)$$

The right-hand side of the above equation, using Eq. (28), can be shown to be $\sim \{M(r - 2M_1)/a^2\}$, which vanishes near the wormhole throat located at $r = 2M_1$. Thus, it follows that near the throat the right-hand side of Eq. (32) is ignorable, while the radion incarnation Φ is only dominant near the throat. Then we can ignore the right-hand side term in Eq. (32) and get the following approximate solution for $\Phi(r)$:

$$\Phi(r) \approx \frac{\Phi_1^2}{4} \left(1 - \frac{4MM_1}{a^2} \right) \ln \left(\chi + \sqrt{1 - \frac{2M_1}{r}} \right)^2$$

$$+ \Phi_1 \sqrt{\Phi_0 + 1} \left(1 - \frac{2MM_1}{a^2} \right) \ln \left(\chi + \sqrt{1 - \frac{2M_1}{r}} \right)$$

$$+ \Phi_0. \quad (33)$$

As evident, structurally, the field Φ in the context of the galactic braneworld wormhole is identical to the isolated wormhole scenario, but a comparison with Eq. (23) reveals that, in the presence of galactic matter, the field Φ is simply getting rescaled.

2. Properties of the galactic braneworld wormhole

The above discussion provides a closure to the discussion involving the geometry of the galactic braneworld wormhole. The detailed expressions for the energy density $\rho^{(g)}$ and transverse pressure $p_{\perp}^{(g)}$ can also be obtained from Einstein's equations, which we will not present here due to the complicated nature of the corresponding expressions. Before concluding this section, we present below the shadow radius and the radius of the ISCO for the galactic braneworld wormhole and compare it with the isolated case. As stated earlier, to mimic galactic observation, we will restrict ourselves in the parameter space such that $a > M \gg M_1$ and $\chi \gtrsim 0$, so that we keep terms up to $\mathcal{O}(1/a^2)$ and linear order in χ , in what follows. Using this approximation, the radii of the photon sphere and the ISCO are given by

$$r_{\text{ph}} = 3M_1 \left(1 + \frac{MM_1}{a^2} \right) - \sqrt{3}\chi M_1, \quad (34)$$

$$r_{\text{ISCO}} = 6M_1 \left(1 - \frac{32MM_1}{a^2} \right) - 3\sqrt{\frac{3}{2}}\chi M_1. \quad (35)$$

The presence of galactic matter places the photon sphere r_{ph} at a larger radius, while the exotic material at the throat decreases the position of the photon sphere. Therefore, a competition between galactic matter and wormhole matter exists, and the photon sphere of a galactic braneworld wormhole is at a larger radius than the isolated wormhole counterpart. From the above expression of r_{ISCO} , it is clear that, in the presence of a galaxy, the ISCO location decreases compared to the isolated wormhole counterpart. Similarly, one can compute the location of the shadow radius for the galactic braneworld wormhole, given by

$$r_{\text{sh}} = 3\sqrt{3}M_1 \left[\left(1 + \frac{M}{a} \right) (1 + (1 - \sqrt{3})\chi) + \frac{M(5M - 18M_1)}{6a^2} \right]. \quad (36)$$

Both the photon sphere and the shadow radii are plotted in Fig. 3, against the dimensionless galactic scale (M/a). The figure explicitly demonstrates how the photon sphere and the shadow radius are affected by the presence of a galaxy; in particular, it follows that the presence of a dark matter halo increases the radii compared to the isolated wormhole counterpart.

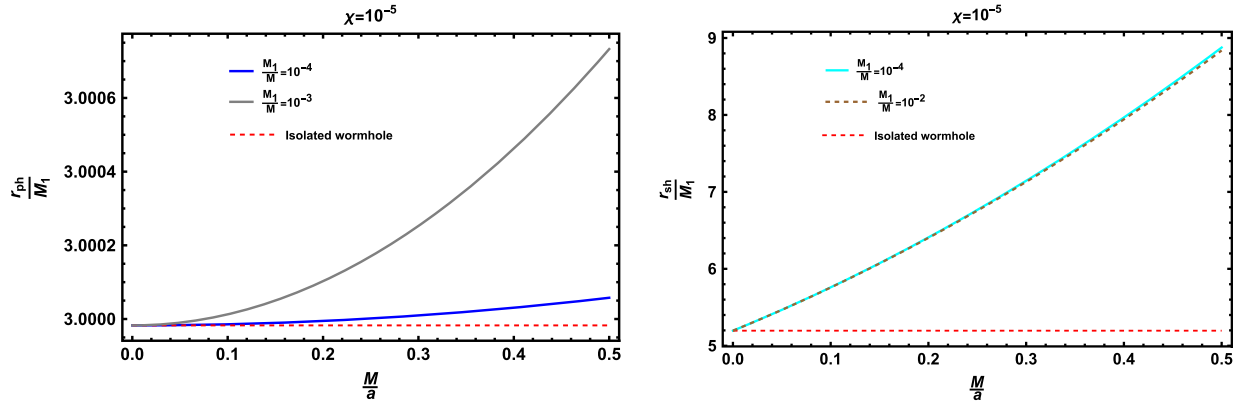


FIG. 3. The radial location of the photon sphere r_{ph} has been presented as a function of the compactness of the galaxy described by the ratio (M/a) on the left. The plot shows that, in the presence of a galaxy, the radial location of the photon sphere increases compared to that of the isolated wormhole. On the other hand, the right panel demonstrates the variation of the shadow radius r_{sh} of galactic braneworld wormhole as a function of the galactic compactness (M/a). This plot also depicts a similar behavior, i.e., in the presence of a galaxy the shadow radius increases compared to its isolated counterpart. In both cases, all the radii are scaled by the ADM mass of the wormhole M_1 .

III. STABILITY OF GALACTIC WORMHOLES UNDER SCALAR PERTURBATION

In this section, we will study the stability of the galactic wormhole spacetimes derived in the previous sections, under external scalar perturbation. In particular, we wish to study how a massless scalar field Ψ evolves in the background geometry, presented in Secs. II A and II B, with appropriate mass profiles for the dark matter environment in the context of the Damour-Solodukhin wormhole, as well as in the braneworld scenario, respectively. We will assume that the energy density of the scalar field Ψ is small, such that it can be ignored compared to the energy densities of various matter species appearing in the galactic wormhole spacetimes. Thus, the scalar field Ψ can be considered as a test scalar field, living in the background geometry of the galactic wormholes and satisfying the massless Klein-Gordon equation, $g^{\mu\nu}\nabla_\mu\nabla_\nu\Psi = 0$. For the metric $g_{\mu\nu}$, we can exploit the result that it describes a static and spherically symmetric geometry, such that the scalar field admits the following decomposition:

$$\Psi(t, r, \theta, \phi) = \frac{1}{r} \sum_{l=0}^{\infty} \sum_{m=-l}^l e^{-i\omega t} Y_{lm}(\theta, \phi) \psi_{lm}(r), \quad (37)$$

where $Y_{lm}(\theta, \phi)$ corresponds to the spherical harmonics and $\psi_{lm}(r)$ is the radial function that needs to be determined. Until this point, we have not used any explicit form for the metric, describing the background spacetime. Substituting the above decomposition for the scalar field Ψ in the massless Klein-Gordon equation, along with the metric ansatz from Eq. (5), we obtain the following equation satisfied by the radial part ψ_{lm} of the scalar field:

$$\frac{d^2\psi_{lm}}{dr_*^2} + \left[\omega^2 - V_l(r)\right]\psi_{lm} = 0. \quad (38)$$

Here we have defined the tortoise coordinate r_* as the solution of the following differential equation:

$$\frac{dr_*}{dr} = \frac{1}{\sqrt{g^{rr}g_{tt}}} = \sqrt{\frac{r}{f(r)[r - 2m(r)]}}, \quad (39)$$

and the potential $V_l(r)$ is given by

$$V_l(r) = f(r) \frac{l(l+1)}{r^2} + \frac{\sqrt{f(r)[1 - 2m(r)/r]}}{r} \times \partial_r \left(\frac{\sqrt{f(r)[1 - 2m(r)/r]}}{r} \right). \quad (40)$$

To proceed further and to obtain the characteristic quasi-normal mode frequencies of the galactic wormhole spacetimes, we need to provide explicit expressions for the mass function and the function $f(r)$, which depends on the specifics of the solution considered and will differ from the galactic Damour-Solodukhin wormhole to the galactic braneworld wormhole. Thus, in what follows, we present the stability analysis of these two galactic wormhole spacetimes separately.

A. Stability of the galactic Damour-Solodukhin wormhole

We start by discussing the stability of the galactic Damour-Solodukhin wormhole spacetime. In this case, the mass profile $m(r)$ is given by Eq. (8) and the g_{tt} component is given by Eq. (12). Substituting both of these expressions in Eq. (40), the following explicit form of the potential for the galactic Damour-Solodukhin wormhole can be obtained (the variation of the potential with the radial coordinate has been presented in Fig. 4):

$$V_l^{(\text{ds})}(r) = \frac{e^\gamma}{r^2(a+r)^3} [V_0(r) + \lambda^2 V_\lambda(r)], \quad (41)$$

where γ has been defined in Eq. (12), and the expressions for the functions $V_0(r)$ and $V_\lambda(r)$, respectively, are given by

$$V_0 = 2 \left(1 - \frac{2M_1}{r} \right) \left[M(r - 2M_1)(r - 4M_1) + \left(\frac{M_1}{r} + \frac{l(l+1)}{2} \right) (r+a)^3 - 2aMM_1 \left(1 - \frac{2M_1}{r} \right) \right], \quad (42)$$

$$V_\lambda = \frac{M_1}{r} \left[\left(1 - \frac{4M_1}{r} \right) \{ (a+r)^3 - 2Ma(r - 2M_1) \} + 2M(3r - 8M_1)(r - 2M_1) \right]. \quad (43)$$

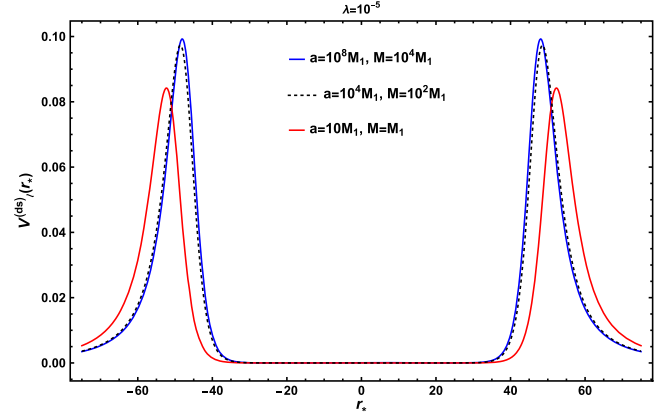


FIG. 4. We have plotted the potential $V_l^{(\text{ds})}$ associated with scalar perturbation of the galactic Damour-Solodukhin wormhole with the tortoise coordinate r_* for different choices of the galactic parameters, with $\ell = 1$. As evident, the total potential $V_l^{(\text{ds})}$ neatly separates into two individual potentials associated with each of the universes at both sides of the throat. The plot of the potential also depicts that, as the ratio (M/a) decreases, both the maxima of the potential increase, while the throat length decreases.

It is possible to provide a simple interpretation for both of these terms V_0 and V_λ —if we had considered a galaxy with a central black hole, then only the term V_0 would appear; on the other hand, the function V_λ appears because the central compact object is a wormhole in the present scenario.

To proceed further, in addition to the potential, we need to provide an explicit expression for the tortoise coordinate r_* as well. Since the determination of the tortoise coordinate involves an integration, there is a constant of integration present in the analysis. We choose the integration constant, keeping in mind that the wormhole geometry connects two universes by a throatlike structure at $r = 2M_2$, such that $r_*(r = 2M_2) = 0$. In this case, we will use $r_* \in (-\infty, \infty)$ to cover both the universes, such that $r \rightarrow \pm\infty$ represents the asymptotic region of both the universes. Using the condition that $a > M \gg M_2 > 0$ and assuming small values of λ , we obtain

$$r_* \simeq \exp \left[\frac{-\beta}{2} \right] \left(1 - \frac{2MM_1}{a^2} \right) \left[r + 2M_1 \ln \left(\frac{r}{2M_1} - 1 \right) \right] + \frac{L}{2}. \quad (44)$$

In the above expression, we have introduced β as a shorthand for the quantity

$$\beta = \sqrt{\frac{M}{2a - M}} \left[2 \tan^{-1} \left(\frac{a - M}{\sqrt{M(2a - M)}} \right) - \pi \right], \quad (45)$$

and L is referred to as the throat length [49] and physically represents the distance between the two maxima of the

perturbing potential, presented in Eq. (41). Therefore, it is a characteristic length scale associated with the scalar perturbation of the galactic Damour-Solodukhin wormhole. An explicit expression for the throat length takes the following form:

$$L = \exp\left[\frac{-\beta}{2}\right] \left(1 - \frac{2MM_1}{a^2}\right) \left[-4M_1 + 4M_1 \ln\left(\frac{4}{\lambda^2}\right)\right], \quad (46)$$

where the last part, which is independent of M , corresponds to the throat length of the isolated Damour-Solodukhin wormhole. Since β is always a negative quantity, it follows that the throat length for a galactic Damour-Solodukhin wormhole is larger than the throat length of an isolated Damour-Solodukhin wormhole (see Fig. 5).

1. Ringdown spectrum of galactic Damour-Solodukhin wormhole

Having laid down all the details regarding the perturbation equation associated with the ringdown spectrum, in this section we will discuss the method for obtaining the quasinormal mode (QNM) frequencies and hence the time domain ringdown signal, which will be compared with the case of an isolated Damour-Solodukhin wormhole. For determining the QNM frequencies, we can replace the double bump potential barrier (as shown in Fig. 4) by two single bump potentials at both sides of the wormhole throat. Each of these single bump potentials can be thought of as the angular momentum barrier associated with the photon sphere of some black hole spacetime. Mathematically this is achieved by expressing the potential due to scalar perturbation as

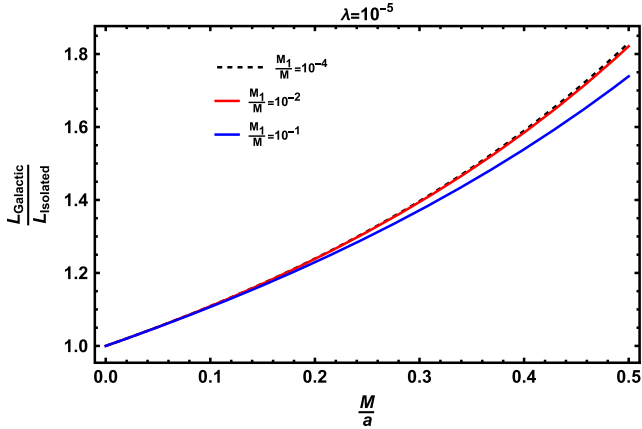


FIG. 5. This plot shows how the presence of a galaxy influences the throat length. Here we have plotted the ratio of throat length between that of the galactic Damour-Solodukhin wormhole and that of the isolated counterpart as a function of $\frac{M}{a}$, for various values of $\frac{M_1}{M}$. From this figure we can see that, in the presence of a galaxy, the throat length of a galactic wormhole always increases from that of an isolated counterpart.

$$V_l^{(\text{ds})}(r_*) = \theta(r_*)V_{l(\text{single})}\left(r_* - \frac{L}{2}\right) + \theta(-r_*)V_{l(\text{single})}\left(-r_* - \frac{L}{2}\right), \quad (47)$$

where $V_{l(\text{single})}(r_*)$ is the single bump potential, entering the following differential equation:

$$\frac{d^2\tilde{\psi}_{lm}}{dr_*^2} + \left[\omega^2 - V_{l(\text{single})}(r_*)\right]\tilde{\psi}_{lm} = 0. \quad (48)$$

Here $\tilde{\psi}_{lm}(r_*, \omega)$ is the master variable if we consider only one universe on either side of the wormhole throat located at $r_* = 0$. From the above structure of the potential V_l , it follows that $V_{l(\text{single})}(r_*)$ vanishes at both the asymptotic and in the near throat region, yielding the following nature for the perturbation $\tilde{\psi}_{lm}(r_*, \omega)$:

$$\tilde{\psi}_{lm}(r_*, \omega) = \begin{cases} Ae^{-i\omega r_*} + Be^{i\omega r_*} & \text{for } r_* \rightarrow \infty, \\ Ce^{-i\omega r_*} + De^{i\omega r_*} & \text{for } r_* \rightarrow 0. \end{cases} \quad (49)$$

Note that here $r_* \rightarrow 0$ does not correspond to the horizon, but rather the near throat region, so that both the ingoing and the outgoing modes will exist. Further, it follows that $V_{l(\text{single})}(r_*)$ becomes $\mathcal{O}(\lambda^2)$ at the location of the throat, i.e., at $r = 2M_2$, which is several orders of magnitude smaller than the frequency ω and hence we can approximate $\sqrt{\omega^2 - V_{l(\text{single})}(0)} \approx \omega$. At this point, we introduce the (2×2) transfer matrix T such that it relates the near throat and asymptotic amplitudes of the incoming and outgoing waves in the region $r_* > 0$, yielding

$$\begin{pmatrix} B \\ A \end{pmatrix} = T \begin{pmatrix} D \\ C \end{pmatrix}. \quad (50)$$

The above coefficients appearing with the ingoing and the outgoing wave modes can be further constrained by imposing appropriate boundary conditions consistent with the QNMs, which correspond to the fact that there are no incoming waves from the asymptotic regions of both universes. For the universe with $r_* > 0$, this condition is manifested by setting $A = 0$ in Eq. (50), which leads to the condition

$$\frac{C}{D} \equiv R_{(\text{single})}(\omega) = -\frac{T_{21}}{T_{22}}. \quad (51)$$

Here $R_{(\text{single})}(\omega)$ is the reflectivity of the single bump potential when probed from the throat toward the asymptotic region. Similarly, one can study the scattering problem associated with the universe having $r_* < 0$. In this context as well, there exists a single bump potential on the negative r_* axis (see Fig. 4), for which the notion of the ingoing and

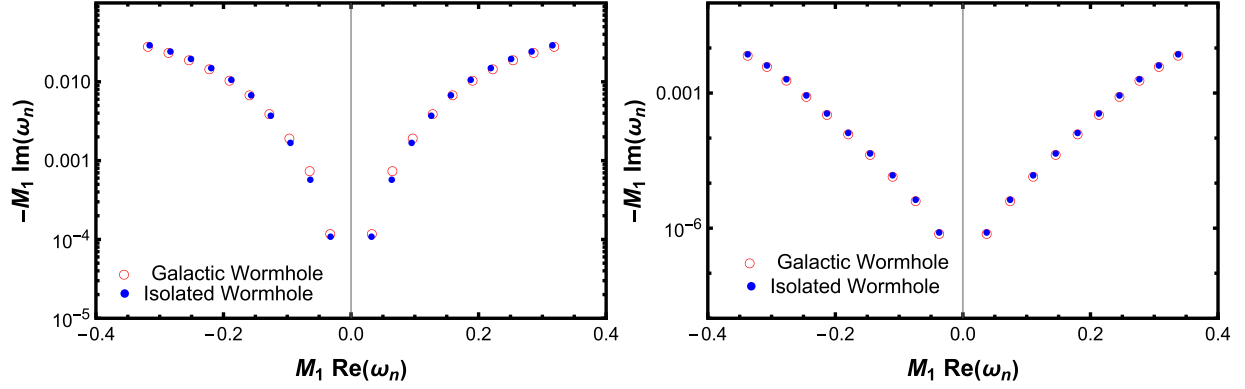


FIG. 6. The real and the imaginary parts of the QNM frequencies of the galactic Damour-Solodukhin wormhole has been depicted on the left for $\ell = 0$, with the metric parameters chosen to be $a = 10^8 M_1$, $M = 10^4 M_1$, and $\lambda = 10^{-5}$. Whereas the plot to the right describes the real and the imaginary parts of the QNM frequencies for $\ell = 1$ with identical choices of the metric parameters.

the outing modes reverses with respect to that of $r_* > 0$. Keeping this in mind, one can find the transfer matrix \tilde{T} for the universe with $r_* < 0$ by using the transfer matrix T associated with the universe having $r_* > 0$, which is given by

$$\tilde{T} = \sigma_x T^{-1} \sigma_x. \quad (52)$$

We now have both the transfer matrices associated with the two universes separately; as a final step we need to match the near throat amplitudes of both universes to obtain the full transfer matrix (\mathbb{T}) for the scattering problem associated with the potential $V_l^{(\text{ds})}(r_*)$. This yields

$$\mathbb{T} = T \begin{pmatrix} e^{i\omega L} & 0 \\ 0 & e^{-i\omega L} \end{pmatrix} \tilde{T}, \quad (53)$$

where the matrix in the middle is a simple translation matrix, relating the amplitudes of outgoing and ingoing modes beyond the single bump potential in one universe to that in another. As already emphasized above, the role of this transfer matrix is to relate the asymptotic amplitudes of the universe with $r_* > 0$ to that of asymptotic amplitudes of the universe with $r_* < 0$.

Since we have already imposed the condition that there are no incoming waves from $r_* = +\infty$, it is time to impose the other condition that there are no incoming waves from $r_* = -\infty$ as well, which demands $\mathbb{T}_{22} = 0$. We obtain the following condition from Eq. (53):

$$e^{-i\omega_n L} = -e^{-in\pi} R_{(\text{single})}(\omega), \quad n = 1, 2, \dots, \quad (54)$$

where L is the throat length and $R_{(\text{single})}(\omega)$ is the reflectivity of a single bump potential. The solution of the above equation yields the associated QNM frequencies. For determining the QNM frequencies, we first find out the reflectivity of the single bump potential numerically and then use Eq. (54). The result of this analysis has been

presented in Fig. 6 as well as in Tables I and II. In particular, Fig. 6 depicts explicitly the real and imaginary parts of the QNM frequencies for the galactic Damour-Solodukhin wormhole spacetime, which we have compared with that of an isolated Damour-Solodukhin wormhole. We observe that the order of magnitudes of the real and the imaginary parts of the QNM frequencies of the galactic Damour-Solodukhin wormhole are in consonance with that of the isolated Damour-Solodukhin wormhole. However, the imaginary parts of the QNM frequencies for galactic Damour-Solodukhin wormholes are larger than their isolated counterpart, implying that, in the presence of a galaxy, the wormhole is more stable than its isolated counterpart.

TABLE I. A comparison of the dimensionless QNM frequencies between the isolated and the galactic Damour-Solodukhin wormhole has been presented for $l = 0$ and $\lambda = 10^{-5}$. The galactic parameters are chosen as $a = 10^8 M_1$ and $M = 10^4 M_1$. As evident from the table, within the same precision, the real part of the QNM frequencies of both wormholes are in agreement, but the magnitude of the imaginary part of the QNM frequencies for the galactic Damour-Solodukhin wormhole is slightly larger than that of the isolated one, suggesting that the galactic Damour-Solodukhin wormhole is more stable than the isolated one.

Comparison of QNM frequencies		
Mode n	For isolated wormhole	For galactic wormhole
1	$0.0321 - 1.083 \times 10^{-4}i$	$0.0326 - 1.2174 \times 10^{-4}i$
2	$0.0638 - 5.720 \times 10^{-4}i$	$0.0649 - 7.6526 \times 10^{-4}i$
3	$0.0950 - 1.679 \times 10^{-3}i$	$0.0967 - 1.9841 \times 10^{-3}i$
4	$0.1258 - 3.709 \times 10^{-3}i$	$0.1280 - 4.0441 \times 10^{-3}i$
5	$0.1566 - 6.739 \times 10^{-3}i$	$0.1592 - 7.0129 \times 10^{-3}i$
6	$0.1877 - 1.0106 \times 10^{-2}i$	$0.1906 - 1.0746 \times 10^{-2}i$
7	$0.2192 - 1.490 \times 10^{-2}i$	$0.2222 - 1.4990 \times 10^{-2}i$
8	$0.2510 - 1.948 \times 10^{-2}i$	$0.2541 - 1.9518 \times 10^{-2}i$
9	$0.2832 - 2.418 \times 10^{-2}i$	$0.2862 - 2.4185 \times 10^{-2}i$
10	$0.3158 - 2.90 \times 10^{-2}i$	$0.3185 - 2.8916 \times 10^{-2}i$

TABLE II. A comparison between the real and the imaginary parts of the QNM frequencies of the isolated and the galactic Damour-Solodukhin wormhole has been presented for $\ell = 1$ and $\lambda = 10^{-5}$. The galactic parameters are chosen as $a = 10^8 M_1$ and $M = 10^4 M_1$. In this case also the values are more or less in agreement, with the galactic wormhole being more stable than the isolated one.

Comparison of QNM frequencies		
Mode n	For isolated wormhole	For galactic wormhole
1	$0.0372 - 7.9961 \times 10^{-7}i$	$0.0372 - 8.0010 \times 10^{-7}i$
2	$0.0741 - 4.2698 \times 10^{-6}i$	$0.0741 - 4.2730 \times 10^{-6}i$
3	$0.1102 - 1.4880 \times 10^{-5}i$	$0.1102 - 1.4893 \times 10^{-5}i$
4	$0.1455 - 4.5449 \times 10^{-5}i$	$0.1455 - 4.5498 \times 10^{-5}i$
5	$0.1798 - 1.2987 \times 10^{-4}i$	$0.1798 - 1.3002 \times 10^{-4}i$
6	$0.2132 - 3.5057 \times 10^{-4}i$	$0.2132 - 3.5103 \times 10^{-4}i$
7	$0.2455 - 8.8235 \times 10^{-4}i$	$0.2455 - 8.8357 \times 10^{-4}i$
8	$0.2767 - 2.0175 \times 10^{-3}i$	$0.2768 - 2.0202 \times 10^{-3}i$
9	$0.3072 - 4.0814 \times 10^{-3}i$	$0.3073 - 4.0865 \times 10^{-3}i$
10	$0.3375 - 7.2239 \times 10^{-3}i$	$0.3375 - 7.2318 \times 10^{-3}i$

This is also evident from both Tables I and II for different choices of the angular number l .

To obtain the time domain signal for the ringdown profile of the galactic Damour-Solodukhin wormhole, we need to analyze the evolution of the scalar perturbation in the time domain. For this purpose, we need to define the Fourier counterpart of $\psi_{lm}(r_*, \omega)$ in the usual manner. Using the perturbation in the time domain and the fact that, for a static and spherically symmetric spacetime, the effective potential appearing in Eq. (38) is frequency independent, we can rewrite the radial perturbation equation, presented in Eq. (38), in the time domain as follows:

$$-\frac{\partial^2 \psi_{lm}(r_*, t)}{\partial t^2} + \frac{\partial^2 \psi_{lm}(r_*, t)}{\partial r_*^2} - V_l^{(ds)}(r_*) \psi_{lm}(r_*, t) = 0. \quad (55)$$

This is a second-order partial differential equation in r_* and t , and hence to solve this equation, one must specify two initial conditions in time and two boundary conditions in the tortoise coordinate. The outgoing boundary conditions at two asymptotic infinities can be implemented as $\partial_{r_*} \psi_{lm}(r_*, t) = \mp \partial_t \psi_{lm}(r_*, t)$, as $r_* \rightarrow \pm\infty$. Whereas we choose the following initial conditions:

$$\psi_{lm}(r_*, 0) = 0 \quad \text{and} \quad \partial_t \psi_{lm}(r_*, 0) = e^{-\frac{(r_* - r_*^0)^2}{\sigma^2}}, \quad (56)$$

where r_*^0 and σ^2 will be chosen in such a way that the primary signal appears outside of the unstable photon sphere, i.e., the maxima of the single bump potential. Using these boundary and initial conditions, we solve Eq. (55) numerically. The result of this analysis can be found from both Figs. 7 and 8, where we have shown the ringdown waveform in the time domain, which consists of

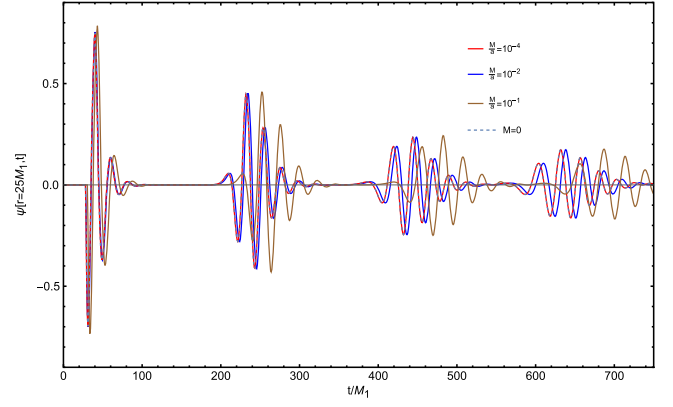


FIG. 7. The time domain ringdown waveform for scalar perturbation has been presented for galactic and isolated Damour-Solodukhin wormholes at $r = 25M_1$ for $\ell = 1$ with $\lambda = 10^{-5}$. We have chosen various values of $\frac{M}{a}$ for the galactic wormhole. In this case, $M = 0$ corresponds to the isolated wormhole. From the plot, one can see that, except for $\frac{M}{a} = 10^{-1}$, the primary signal of the waveform matches very well with the isolated wormhole. Moreover, the late-time echoes give us the scope to determine the galactic parameters via the echo time delay. The parameters appearing in the initial Gaussian profile [see Eq. (56)] are chosen such that r_*^0 is larger than the location of the photon sphere and $\sigma = 10M_1$. Using this choice, we have numerically solved the time domain wave equation and presented it here.

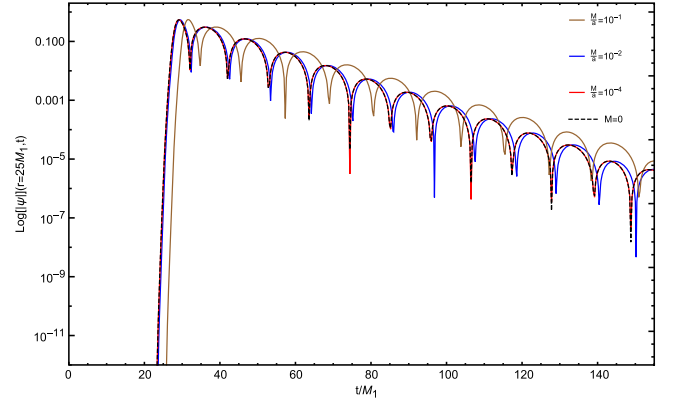


FIG. 8. To distinguish the prompt ringdown signal in the waveform of the galactic Damour-Solodukhin wormhole from that of an isolated wormhole, we have plotted the logarithm of the absolute value of the ringdown signal for $l = 1$ with $\lambda = 10^{-5}$ at $r = 25M_1$. The parameters of the plot are chosen such that $\sigma = M_1$ and r_*^0 is larger than the photon sphere. From the plot, one can see that, except for large (M/a) ratio for the galactic matter, e.g., $\frac{M}{a} = 10^{-1}$, the primary signal of the waveform matches very well with that of the isolated wormhole.

echoes of the primary signal due to repetitive reflection of the primary signal between the two maxima of the potential $V_l^{(ds)}(r_*)$. The time delay between two successive echoes is given by $\Delta t = 2L$. As in the presence of galactic matter, the throat length increases and, as a consequence, the time

delay also increases. This can be seen explicitly from Eq. (46). Therefore, if echoes are observed in the time domain waveform, they can provide crucial hints not only for the central wormhole, but also about the dark matter halo surrounding it.

B. Ringdown profile and stability of galactic braneworld wormhole

In this section, we will present the QNM frequencies and the ringdown profiles in the time domain using the method introduced in Sec. III A 1, but for the galactic braneworld wormhole. In this case, also the evolution of the perturbing scalar field Ψ is described by the massless Klein-Gordon equation, but we have to make an additional assumption that the energy density of the field Ψ is much smaller than the energy density of the background radion incarnation Φ , loosely speaking $|\Psi| \ll |\Phi|$ (see [41] for further details). As in the previous case, here also the potential experienced by the scalar perturbation Ψ can be expressed in terms of galactic as well as wormhole parameters. However, the potential has a very complicated structure, and hence we have delegated its analytic expression to Appendix D. However, the structure of the potential has been plotted in Fig. 9 for different choices of the galactic parameters, and as evident from the plots, as the dimensionless ratio (M/a) decreases the distance between the maxima decreases while the maxima themselves increase. The tortoise coordinate used in the master equation will be chosen in such a way that $r_*(r = 2M_1) = 0$, and we will have $r_* \in (-\infty, +\infty)$ to cover both the asymptotically flat spacetimes on each side of the throat. As in the previous scenario, for the case of the

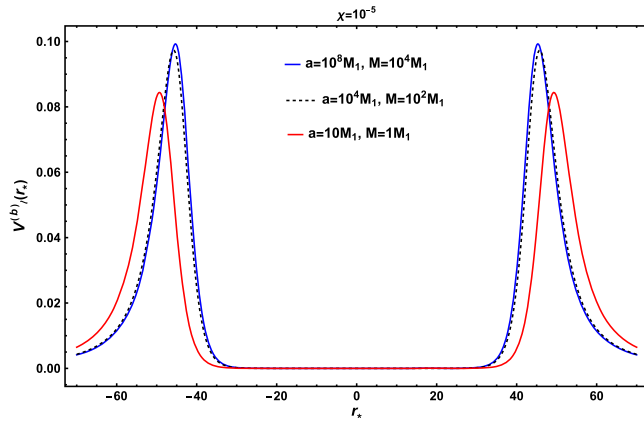


FIG. 9. We have plotted the potential $V_l^{(b)}$ associated with scalar perturbation of the galactic braneworld wormhole with the tortoise coordinate r_* for different choices of the galactic parameters, with $\ell = 1$. As evident, the total potential $V_l^{(b)}$ neatly separates into two individual potentials associated with each of the universes at both sides of the throat. The plot of the potential also depicts that, as the ratio (M/a) decreases, both the maxima of the potential increase and the distance between the two maxima decreases.

braneworld wormhole as well we can not provide an explicit analytic expression for the tortoise coordinate in terms of the radial coordinate r ; however, assuming $a > M \gg M_1 > 0$ and $\chi \gtrsim 0$, we obtain

$$r_* \simeq \exp\left[\frac{-\beta}{2}\right] \left(1 - \frac{2MM_1}{a^2}\right) \left[r + 2M_1 \ln\left(\frac{r}{2M_1} - 1\right)\right] + \frac{\tilde{L}}{2}. \quad (57)$$

The quantity β has already been defined in Eq. (45) and the throat length \tilde{L} is given by

$$\tilde{L} = -4M_1 \exp\left[\frac{-\beta}{2}\right] \left(1 - \frac{2MM_1}{a^2}\right) (1 + 2 \ln \chi). \quad (58)$$

Since the wormhole parameter χ is taken to be smaller than unity, the throat length is actually positive. Also, similar to the case of a galactic Damour-Solodukhin wormhole, in the case of a galactic braneworld wormhole the throat length increases in the presence of a galactic halo, see Fig. 10.

Having outlined the basic setup for the scalar perturbation, one can express the effective potential $V_l^{(b)}$ for the galactic braneworld wormhole in terms of two single bump potentials appearing on both sides of the wormhole throat. Thus, one can employ the same techniques as in the previous section and shall finally obtain the QNM frequencies by solving Eq. (54) with the reflectivity due to the appropriate potential for the galactic braneworld wormhole. Here also we numerically solve for the reflectivity and hence obtain the QNM frequencies, which have been presented in Fig. 11 and Table III. In Fig. 11, besides presenting the real and imaginary parts of the QNM

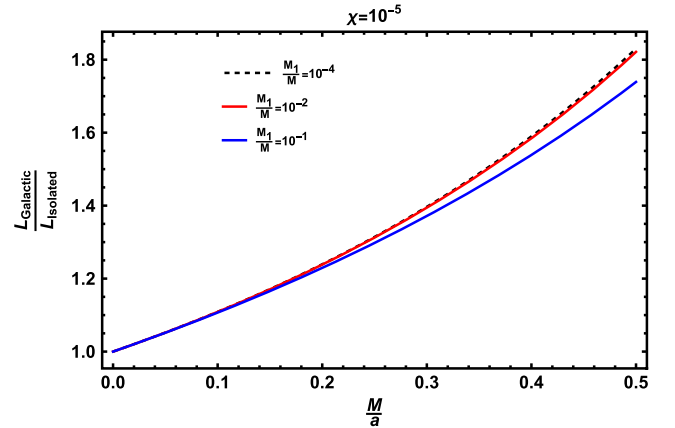


FIG. 10. This plot shows how the presence of a galaxy influences the throat length of the braneworld wormhole. Here we have plotted the ratio of throat length between that of the braneworld galactic wormhole and that of the isolated counterpart as a function of $\frac{M}{a}$, for various values of $\frac{M_1}{M}$. From this figure, we can see that, in the presence of a galaxy, the throat length of a galactic wormhole always increases from that of an isolated counterpart, as in the case of the Damour-Solodukhin wormhole.

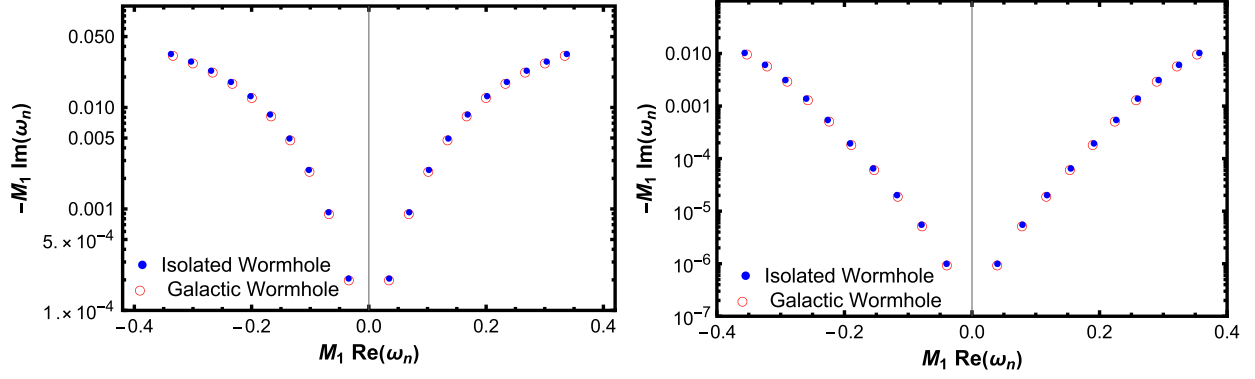


FIG. 11. On the left we have plotted the QNM frequencies for the $\ell = 0$ mode of the scalar perturbation on the galactic and isolated braneworld wormhole with metric parameters chosen to be $a = 10^4 M_1$, $M = 10^2 M_1$, and $\chi = 10^{-5}$. Whereas the right-hand side plot of the QNM frequencies is for the same systems, but with $\ell = 1$ with metric parameters chosen to be $a = 10^4 M_1$, $M = 10^2 M_1$, and $\chi = 10^{-5}$.

frequencies associated with the scalar perturbation of the galactic braneworld wormhole, we have also presented the real and imaginary parts of the QNM frequencies of the isolated braneworld wormhole. As evident, the QNM frequencies associated with scalar perturbation of both of these spacetimes have the same order, but their imaginary parts differ in magnitude. In particular, the imaginary part of the QNM frequency of a braneworld wormhole in a galaxy will be smaller than the isolated one, and hence it follows that the isolated braneworld wormhole is more stable compared to the galactic wormhole. This is in contrast to the Damour-Solodukhin wormhole. Finally, the determination of the ringdown waveform in the time domain can be obtained by using the method outlined in Sec. III A 1 with appropriate boundary and initial

TABLE III. We have presented a comparison of the QNM frequencies between the isolated and the galactic braneworld wormhole for $\ell = 1$ and $\chi = 10^{-5}$. The galactic parameters are chosen as $a = 10^4 M_1$ and $M = 10^2 M_1$. From the above table it is clear that, within the same precision, the magnitude of the imaginary part of the QNM frequencies of the isolated wormhole is slightly larger than that of the galactic one. Therefore, the isolated wormhole is more stable than the galactic one.

Comparison of the QNM frequencies		
Mode n	For isolated wormhole	For galactic wormhole
1	$0.0398 - 9.9449 \times 10^{-7}i$	$0.0394 - 9.8454 \times 10^{-7}i$
2	$0.0792 - 5.5084 \times 10^{-6}i$	$0.0784 - 5.4532 \times 10^{-6}i$
3	$0.1176 - 2.0163 \times 10^{-5}i$	$0.1164 - 1.9961 \times 10^{-5}i$
4	$0.155 - 6.4867 \times 10^{-5}i$	$0.1534 - 6.4218 \times 10^{-5}i$
5	$0.1912 - 1.9426 \times 10^{-4}i$	$0.1893 - 1.9232 \times 10^{-4}i$
6	$0.2262 - 5.4270 \times 10^{-4}i$	$0.2239 - 5.3728 \times 10^{-4}i$
7	$0.2599 - 1.3837 \times 10^{-3}i$	$0.25733 - 1.3699 \times 10^{-3}i$
8	$0.2926 - 3.1189 \times 10^{-3}i$	$0.2896 - 3.0878 \times 10^{-3}i$
9	$0.3246 - 6.0766 \times 10^{-3}i$	$0.3213 - 6.0157 \times 10^{-3}i$
10	$0.3565 - 1.0247 \times 10^{-2}i$	$0.3529 - 1.0145 \times 10^{-2}i$

conditions. The result of such an analysis has been presented in Figs. 12 and 13. As evident for these plots, the echoes are sensitive to even small values of the ratio (M/a) , however, the prompt ringdown only gets affected for $(M/a) \sim 10^{-1}$.

IV. DISCUSSION

Wormholes are exotic objects, which can be as compact as that of black holes, but without any event horizon. Since wormhole geometries involve the photon sphere, the

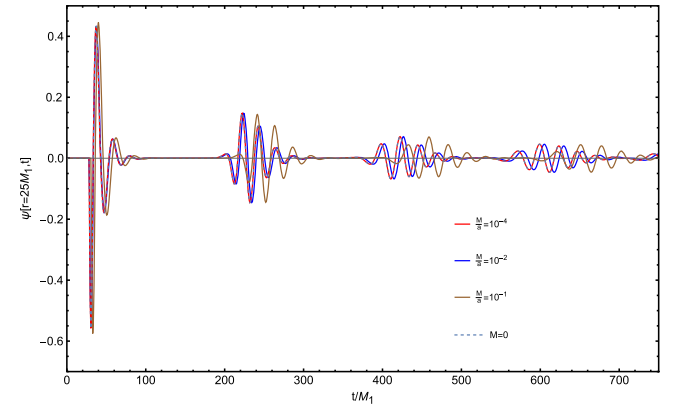


FIG. 12. The time domain ringdown waveform for scalar perturbation has been presented for galactic and isolated braneworld wormhole at $r = 25 M_1$ for $\ell = 1$ with $\chi = 10^{-5}$. For the galactic wormhole, we have chosen various values of $\frac{M}{a}$. In this case, $M = 0$ corresponds to the isolated wormhole. From the plot, one can see that, except for $\frac{M}{a} = 10^{-1}$, the primary signal of the waveform matches very well with the isolated wormhole. Moreover, the late-time echoes give us the scope to determine the galactic parameters via the echo time delay. The parameters appearing in the initial Gaussian profile [see Eq. (56)] are chosen such that r_*^0 is larger than the location of the photon sphere, and $\sigma = 10 M_1$. Using this choice, we have numerically solved the time domain wave equation and presented it here.

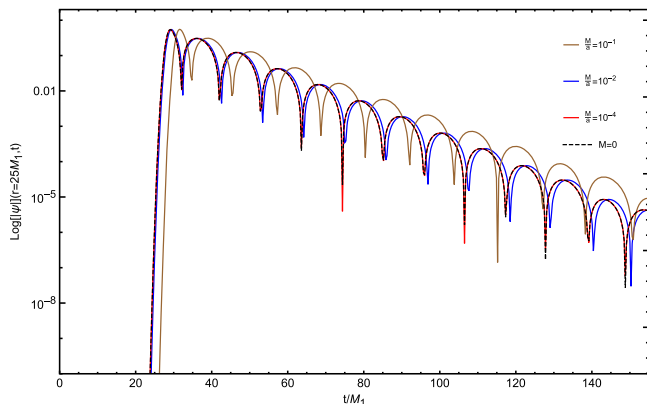


FIG. 13. To distinguish the primary signal in the ringdown waveform of a galactic braneworld wormhole from that of an isolated wormhole, we have plotted the logarithm of the absolute value of the ringdown signal for $l = 1$ with $\chi = 10^{-5}$ at $r = 25M_1$. The parameters of the plot are chosen such that $\sigma = 1M_1$, and r_*^0 is larger than the photon sphere. From the plot, one can see that, except for $\frac{M}{a} = 10^{-1}$, the primary signal of the waveform matches very well with the isolated wormhole.

prompt ringdown of the GW waveform can be mimicked by them, but modifications will come in at later times, with the introduction of echoes in the time domain signal. There has been extensive discussion involving such ECOs regarding their origin, stability, and response under various external perturbations of scalar, electromagnetic, and gravitational origin. However, all such discussions were in the context of isolated systems. In this work we have made the first attempt to incorporate environmental effects, mainly that of the surrounding dark matter halo, on the geometry of certain wormhole spacetimes. We hope our strategy will be useful for embedding other ECOs in the surrounding dark matter halo, as well.

We have used two distinct wormhole solutions for our purpose: (a) the Damour-Solodukhin wormhole and (b) the braneworld wormhole. In both cases, we could provide a suitable mass profile, which predicts wormhole matter distribution at small radii and a Hernquist-type galactic mass profile at a larger radius. Astonishingly, the galactic wormholes, be it Damour-Solodukhin or braneworld, have their throat at exactly the same location as that of their isolated counterpart. Moreover, the presence of galactic matter tames the violation of the energy conditions significantly. For example, in the context of an isolated Damour-Solodukhin wormhole the null and the strong energy conditions are violated everywhere, whereas for the galactic Damour-Solodukhin wormhole, the violations of the energy conditions happen in a very small region close to the throat of the wormhole. This result can also be understood in an intuitive manner—near the throat, the properties of the wormhole dominate and hence the energy conditions are violated, while away from the throat, the properties of the galactic matter take over, restoring the energy conditions.

The impact of galactic matter can also be felt on the physical properties of the wormholes, e.g., the location of the photon sphere, ISCO, and shadow radius. In particular, it generically follows that the shadow radius and the photon sphere radius for galactic wormholes are larger than their isolated counterpart. This means galactic wormholes cast a larger shadow. In this respect, it is worth pointing out that the shadow radius of the M87* within the M87 galaxy is larger than what is expected from the dynamics of stars and gases surrounding it. A possible reason for the larger shadow could be due to the presence of a dark matter halo surrounding the same, given our findings regarding the shadow radius in this work.⁴ Similarly, the enhancement of the ISCO radius will also have implications for accretion physics. Since the luminosity arising from the accretion disk is obtained by integrating over the disk, which extends from the ISCO to infinity, an enhancement of the ISCO radius should lower the luminosity. This can lead to different parameter values for the accreting object and may also involve estimations for the galactic parameters as well. We wish to come back to both of these issues in the future.

As the dark matter halo modifies the geometry, it also has a significant impact on the stability of these galactic wormholes. It turns out that the galactic matter modifies the potential experienced by the perturbing scalar field significantly by enhancing the throat length but lowering the maxima of the potential. As a consequence, the prompt ringdown will be affected, as the height of the potential decreases, and the echoes in the time domain signal will also be shifted, since the time delay increases. Both of these effects can be seen from Figs. 7 and 8 for the galactic Damour-Solodukhin wormhole, while Figs. 12 and 13 depict such effects for the galactic braneworld wormhole. Interestingly, the imaginary parts of the QNM frequencies for the galactic Damour-Solodukhin wormhole are higher compared to the QNM frequencies of the isolated Damour-Solodukhin wormhole, indicating that the presence of galactic matter makes the Damour-Solodukhin wormhole more stable. On the other hand, for the galactic braneworld wormhole, we have observed the exact opposite scenario. It is expected that, if echoes are observed in the future generations of GW detectors, then a correlation between the parameters derived from the prompt ringdown and from the time delay can provide indirect evidence for the existence of a dark matter halo. This is because, unlike other models of ECOs, for wormholes, the time delay is related to various parameters of the wormhole geometry and hence is not free. Thus, future generations of GW detectors can possibly be used as an independent probe for identifying the galactic parameters.

⁴Such an enhancement in the shadow radius can also be due to other effects, e.g., the presence of extra dimensions can also enhance the shadow radius through a negative tidal charge parameter [86,87].

In that analysis it turned out that the spacetime is linearly unstable due to existence of exponentially growing mode with time. Now coming back to our context. It turns out that the galactic matter modifies the potential experienced by the perturbing scalar field significantly by enhancing the throat length but lowering the maxima of the potential. As a consequence, the prompt ringdown will be affected, as the height of the potential decreases, and the echoes in the time domain signal will also be shifted, since the time delay increases. Both of these effects can be seen from Figs. 7 and 8 for the galactic Damour-Solodukhin wormhole, while Figs. 12 and 13 depict such effects for the galactic braneworld wormhole. Interestingly, the imaginary parts of the QNM frequencies for the galactic Damour-Solodukhin wormhole are higher compared to the QNM frequencies of the isolated Damour-Solodukhin wormhole, indicating that the presence of galactic matter makes the Damour-Solodukhin wormhole more stable. On the other hand, for the galactic braneworld wormhole, we have observed the exact opposite scenario. It is expected that, if echoes are observed in the future generations of GW detectors, then a correlation between the parameters derived from the prompt ringdown and from the time delay can provide indirect evidence for the existence of a dark matter halo. This is because, unlike other models of ECOs, for wormholes, the time delay is related to various parameters of the wormhole geometry and hence is not free. Thus, future generations of GW detectors can possibly be used as an independent probe for identifying the galactic parameters.

It will be worth to mention here that the stability analysis reported above is due to a test scalar field, which does not affect the background geometry. It is important to perturb the source of the wormhole itself and check for stability. There have been few works in this direction with mixed results—(a) wormhole geometries arising out of phantom matter were shown to be unstable under perturbation of the matter sector [88,89], while (b) there are some wormholes in general relativity that have also been shown to be stable under matter perturbation [90]. It will be interesting to perform a similar study on the wormhole geometries considered here, which we wish to come back to in a future work.

There are several other future directions of exploration possible. In this work, we have employed the Hernquist-type mass profile for describing the galactic wormhole spacetimes, however, a more complete mass profile, e.g., the Navarro-Frenk-White (NFW) profile [77], can also be used. Although, with the use of the NFW mass profile, it would not be possible to obtain any closed-form analytic solutions, they may provide a more realistic description of the impact of dark matter halo on wormhole geometries. Furthermore, we have not discussed the response of these galactic wormhole spacetimes due to external tidal effects. Since it is well known that ECOs, including wormholes, have nonzero tidal Love numbers, it would be interesting to see how much these Love numbers are shifted upon the

inclusion of a dark matter halo surrounding the isolated wormholes. In addition, understanding the influence of environmental factors on the physical properties of other classes of ECOs, including quantum-corrected black holes, will be another interesting avenue to explore. Finally, the effect of accretion on the stability of wormhole geometries remains to be understood. In particular, how accretion shifts the quasinormal mode frequencies and whether it can make the wormhole throat unstable is an interesting direction to explore. We hope to return to these issues elsewhere.

ACKNOWLEDGMENTS

S. B. thanks IACS for financial support and Sayan Kar for the helpful discussion during a meeting. C. S. thanks the Saha Institute of Nuclear Physics (SINP), Kolkata for financial support. C. S. is thankful to IACS for their warm hospitality and research facilities. Research of S. C. is funded by the INSPIRE Faculty fellowship from DST, Government of India (Registration No. DST/INSPIRE/04/2018/000893). A part of this work was completed in the Max-Planck Institute for gravitational Physics at Golm, Germany and S. C. acknowledges the warm hospitality there.

APPENDIX A: AN ALTERNATIVE MASS PROFILE FOR DAMOUR-SOLODUKHIN WORMHOLE

In the main text, we advocated one particular choice of the mass profile for the galactic Damour-Solodukhin wormhole. However, it turns out that there can be other possible choices for the mass profile. In particular, we present below one such alternative mass profile, which reads

$$m(r) = M_2 + \frac{Mr^2}{(r+a)^2} \left(1 - \frac{2M_2}{r}\right)^2. \quad (\text{A1})$$

Using the above mass profile, one can indeed solve the radial Einstein equations, as presented by Eq. (11), which yields the following solution for the g_{tt} component of the metric:

$$f(r) = \frac{\exp G(r)}{r} (r - 2M_1)^{\frac{(a+2M_1)^2}{q}} \times (a^2 + 2ar + 4MM_2 - 2Mr + r^2)^{\frac{2M(M_2-M_1)}{q}}, \quad (\text{A2})$$

where the function $G(r)$ has the following expression:

$$G = \frac{2}{q} \{a^2 + 2a(M_1 + M_2) + 2M(M_2 - M_1) + 4M_1M_2\} \sqrt{\frac{M}{\xi}} F(r);$$

$$F = \tan^{-1} \left(\frac{a - M + r}{\sqrt{M\xi}} \right) - \frac{\pi}{2}, \quad (\text{A3})$$

and the constants ξ and q read as $\xi = 2a - M + 4M_1$ and $q = (a + 2M_1)^2 + 4M(M_2 - M_1)$. Note that this function also vanishes at $r = 2M_1$, but remains nonzero at $r = 2M_2$, signaling the existence of a wormhole throat at $r = 2M_2$. Hence, the basic nature of the galactic Damour-Solodukhin wormhole spacetime remains the same, even with this alternative mass profile. However, due to its complicated functional dependence on the radial coordinate, we have not used it for further analysis.

APPENDIX B: THE TANGENTIAL PRESSURE FOR GALACTIC DAMOUR-SOLODUKHIN WORMHOLE

We have described the energy density of the galactic matter supporting the galactic Damour-Solodukhin wormhole. However, we have not explicitly mentioned the radial dependence of the tangential pressure associated with the wormhole spacetime. Here, for completeness, we present the tangential pressure of the dark matter halo, which reads

$$p_{\perp}^{(g)}(ds) = \frac{1}{16\pi r^2} \left[\frac{2\lambda^2 r M_1}{(r - 2M_1)^2} + \left(\frac{2Mr}{(r+a)^2 - 2M(r-2M_1)} + \frac{2M_1}{r-2M_1} \right) \times \left\{ \frac{2M(\lambda^2 M_1(r-a-4M_1) + (a+2M_1)(r-2M_1))}{(a+r)^3} + \frac{\lambda^2 M_1}{2M_1 - r} \right\} \right]. \quad (\text{B1})$$

Note that, in the limit $\lambda \rightarrow 0$, the above expression coincides with [67]. Moreover, the tangential pressure is positive for any radii $r > 2M_2$.

APPENDIX C: CONSISTENCY OF THE GRAVITATIONAL FIELD EQUATIONS ON THE BRANE

In this section, we will sketch how one can arrive at the field equation for the radion incarnation Φ , starting from the Bianchi identity. In what follows we will assume that the Planck brane is vacuum, such that the effective Einstein equations on the visible brane can be written as

$$\Phi G_{\mu\nu} = \frac{\kappa^2}{\ell} T_{\mu\nu}^{\text{vis}} + T_{\mu\nu}^{\Phi}. \quad (\text{C1})$$

Now operating ∇^{μ} on both sides, we get

$$G_{\mu\nu} \nabla^{\mu} \Phi = \nabla^{\mu} T_{\mu\nu}^{\Phi}. \quad (\text{C2})$$

To arrive at the previous result we have used the contracted Bianchi identity $\nabla^{\mu} G_{\mu\nu} = 0$ and have assumed that $\nabla^{\mu} T_{\mu\nu}^{\text{vis}} = 0$. Now using the identity

$$[\nabla_{\alpha}, \nabla_{\nu}] \nabla_{\mu} \Phi = -R^{\beta}_{\mu\alpha\nu} \nabla_{\beta} \Phi, \quad (\text{C3})$$

one can show that

$$\nabla^{\mu} T_{\mu\nu}^{\Phi} = R_{\mu\nu} \nabla^{\mu} \Phi - \frac{3\nabla_{\nu} \Phi}{2(1+\Phi)} \gamma. \quad (\text{C4})$$

Here we have defined the quantity γ as

$$\gamma \equiv \nabla^{\alpha} \nabla_{\alpha} \Phi - \frac{1}{2(1+\Phi)} \nabla^{\alpha} \Phi \nabla_{\alpha} \Phi. \quad (\text{C5})$$

Using Eq. (C4) in Eq. (C2) we obtain the following relation:

$$\nabla_{\nu} \Phi \left[\frac{3\gamma}{2(1+\Phi)} - \frac{R}{2} \right] = 0. \quad (\text{C6})$$

On the other hand, taking the trace of Eq. (C1) we obtain

$$-R\Phi = \frac{\kappa^2}{\ell} T^{\text{vis}} + T^{\Phi}. \quad (\text{C7})$$

Using the explicit form for the energy-momentum tensor $T_{\mu\nu}^{\Phi}$ of the radion field Φ , one can show that

$$T^{\Phi} = -3\gamma. \quad (\text{C8})$$

Therefore, using Eqs. (C7) and (C8) in Eq. (C6) we can finally arrive at the following differential equation for Φ :

$$\nabla_{\nu} \Phi \left[-\frac{2\omega+3}{2} \gamma + \frac{\kappa^2}{2\ell} T^{\text{vis}} \right] = 0, \quad \omega \equiv -\frac{3\Phi}{2(1+\Phi)}. \quad (\text{C9})$$

The above equation can be satisfied in two possible manners: (a) if Φ is a constant field or (b) if Φ satisfies the following differential equation:

$$\gamma = \frac{\kappa^2}{\ell} \frac{T^{\text{vis}}}{2\omega+3}. \quad (\text{C10})$$

Using the definition of γ from Eq. (C5), as well as the coupling function ω , we get back the field equation of the radion incarnation Φ used in the main text.

APPENDIX D: EFFECTIVE POTENTIAL FOR GALACTIC BRANEWORLD WORMHOLE

The complete expression for the effective potential experienced by a test scalar field living in the galactic braneworld wormhole geometry is given by

$$\begin{aligned}
V_l^{(b)}(r) = & \frac{e^\gamma}{(1+\chi)^2 r^4 (a+r)^3 \sqrt{1-\frac{2M_1}{r}}} \left((a+r)(r-2M_1) \left(\chi + \sqrt{1-\frac{2M_1}{r}} \right) \right. \\
& \times \left(a^2 M_1 + 2aM_1 r + M \left(4M_1^2 + \chi r^2 \sqrt{1-\frac{2M_1}{r}} - 4M_1 r + r^2 \right) + M_1 r^2 \right) \\
& + r \sqrt{1-\frac{2M_1}{r}} \left(\chi + \sqrt{1-\frac{2M_1}{r}} \right)^2 (a^3 M_1 + 3a^2 M_1 r + a(4MM_1^2 - Mr^2 + 3M_1 r^2) \\
& + Mr(12M_1^2 - 8M_1 r + r^2) + M_1 r^3) + l(l+1)r^2(a+r)^3 \sqrt{1-\frac{2M_1}{r}} \left(\chi + \sqrt{1-\frac{2M_1}{r}} \right)^2 \left. \right). \quad (D1)
\end{aligned}$$

As in the case of galactic Damour-Solodukhin wormhole spacetime, in this case as well the effective potential $V_l^{(b)}(r)$ can be approximated as follows:

$$V_l^{(b)}(r) \simeq \frac{e^\gamma}{r^4 (a+r)^3} [V_0 + \chi V_\chi], \quad (D2)$$

where V_0 is the leading-order term independent of the wormhole parameter χ and V_χ is the coefficient of the linear-order term in χ , which are defined as follows:

$$\begin{aligned}
V_0 = & (a+r)(r-2M_1) \left(a^2 M_1 + 2aM_1 r + 2MM_1(2M_1 - r) + Mr(r-2M_1) + M_1 r^2 \right) \\
& + r \left(1 - \frac{2M_1}{r} \right) \left(a^3 M_1 + 3a^2 M_1 r + a(4MM_1^2 - Mr^2 + 3M_1 r^2) + Mr(12M_1^2 - 8M_1 r + r^2) + M_1 r^3 \right) \\
& + l(l+1)r^2(a+r)^3 \left(1 - \frac{2M_1}{r} \right), \quad (D3)
\end{aligned}$$

and

$$\begin{aligned}
V_\chi = & (a+r)(r-2M_1) \left(a^2 M_1 + 2aM_1 r + 2MM_1(2M_1 - r) + 2Mr(r-2M_1) + M_1 r^2 \right) \\
& - 2\sqrt{1-\frac{2M_1}{r}}(r-2M_1) \left(a^3 M_1 + (a+r)(a^2 M_1 + 2aM_1 r + 2MM_1(2M_1 - r) + Mr(r-2M_1) + M_1 r^2) \right. \\
& + 3a^2 M_1 r + l(l+1)r(a+r)^3 + a(4MM_1^2 - Mr^2 + 3M_1 r^2) + Mr(12M_1^2 - 8M_1 r + r^2) + M_1 r^3 \left. \right) \\
& + 2(r-2M_1) \left(a^3 M_1 + 3a^2 M_1 r + a(4MM_1^2 - Mr^2 + 3M_1 r^2) + Mr(12M_1^2 - 8M_1 r + r^2) + M_1 r^3 \right) \\
& + 2l(l+1)r(a+r)^3(r-2M_1). \quad (D4)
\end{aligned}$$

These expressions involving the effective potential experienced by a scalar field have been used in Fig. 9 in the main text.

- [1] G. 't Hooft, *Quantum Gravity: A Fundamental Problem and Some Radical Ideas in Recent Developments in Gravitation*, edited by M. Levi and S. Deser (Plenum, New York/London, 1978).
- [2] T. Ortín, *Gravity and Strings*, Cambridge Monographs on Mathematical Physics (Cambridge University Press, Cambridge, England, 2004).
- [3] C. Rovelli, *Quantum Gravity* (Cambridge University Press, Cambridge, England, 2004).
- [4] M. Bojowald, *Canonical Gravity and Applications* (Cambridge University Press, Cambridge, England, 2010).
- [5] M. Fierz and W. Pauli, On relativistic wave equations for particles of arbitrary spin in an electromagnetic field, *Proc. R. Soc. A* **173**, 211 (1939).
- [6] T. Padmanabhan, From gravitons to gravity: Myths and reality, *Int. J. Mod. Phys. D* **17**, 367 (2008).
- [7] S. Deser, Gravity from self-interaction redux, *Gen. Relativ. Gravit.* **42**, 641 (2010).
- [8] S. N. Gupta, Quantization of Einstein's gravitational field: Linear approximation, *Proc. Phys. Soc. London Sect. A* **65**, 161 (1952).
- [9] E. Berti *et al.*, Testing general relativity with present and future astrophysical observations, *Classical Quantum Gravity* **32**, 243001 (2015).
- [10] C. M. Will, The confrontation between general relativity and experiment, *Living Rev. Relativity* **17**, 4 (2014).
- [11] C. Will and N. Yunes, *Is Einstein Still Right?: Black Holes, Gravitational Waves, and the Quest to Verify Einstein's Greatest Creation* (Oxford University Press, Oxford, 2020).
- [12] B. P. Abbott *et al.* (LIGO Scientific and Virgo Collaborations), Observation of gravitational waves from a binary black hole merger, *Phys. Rev. Lett.* **116**, 061102 (2016).
- [13] B. P. Abbott *et al.* (LIGO Scientific and VIRGO Collaborations), GW170104: Observation of a 50-solar-mass binary black hole coalescence at redshift 0.2, *Phys. Rev. Lett.* **118**, 221101 (2017); **121**, 129901(E) (2018).
- [14] B. P. Abbott *et al.* (LIGO Scientific and Virgo Collaborations), GWTC-1: A gravitational-wave transient catalog of compact binary mergers observed by LIGO and Virgo during the first and second observing runs, *Phys. Rev. X* **9**, 031040 (2019).
- [15] R. Abbott *et al.* (LIGO Scientific and Virgo Collaborations), GWTC-2: Compact binary coalescences observed by LIGO and Virgo during the first half of the third observing run, *Phys. Rev. X* **11**, 021053 (2021).
- [16] R. Abbott *et al.* (LIGO Scientific and Virgo Collaborations), Tests of general relativity with binary black holes from the second LIGO-Virgo gravitational-wave transient catalog, *Phys. Rev. D* **103**, 122002 (2021).
- [17] B. P. Abbott *et al.* (LIGO Scientific and Virgo Collaborations), GW190425: Observation of a compact binary coalescence with total mass $\sim 3.4M_{\odot}$, *Astrophys. J. Lett.* **892**, L3 (2020).
- [18] A. Almheiri, D. Marolf, J. Polchinski, and J. Sully, Black holes: Complementarity or firewalls?, *J. High Energy Phys.* **02** (2013) 062.
- [19] S. D. Mathur, The fuzzball proposal for black holes: An elementary review, *Fortschr. Phys.* **53**, 793 (2005).
- [20] Q. Wang, N. Oshita, and N. Afshordi, Echoes from quantum black holes, *Phys. Rev. D* **101**, 024031 (2020).
- [21] I. Agullo, V. Cardoso, A. D. Rio, M. Maggiore, and J. Pullin, Potential gravitational wave signatures of quantum gravity, *Phys. Rev. Lett.* **126**, 041302 (2021).
- [22] S. Chakraborty, E. Maggio, A. Mazumdar, and P. Pani, Implications of the quantum nature of the black hole horizon on the gravitational-wave ringdown, *Phys. Rev. D* **106**, 024041 (2022).
- [23] V. Cardoso, L. C. B. Crispino, C. F. B. Macedo, H. Okawa, and P. Pani, Light rings as observational evidence for event horizons: Long-lived modes, ergoregions and nonlinear instabilities of ultracompact objects, *Phys. Rev. D* **90**, 044069 (2014).
- [24] V. Cardoso, E. Franzin, and P. Pani, Is the gravitational-wave ringdown a probe of the event horizon?, *Phys. Rev. Lett.* **116**, 171101 (2016).
- [25] V. Cardoso, S. Hopper, C. F. B. Macedo, C. Palenzuela, and P. Pani, Gravitational-wave signatures of exotic compact objects and of quantum corrections at the horizon scale, *Phys. Rev. D* **94**, 084031 (2016).
- [26] V. Cardoso and P. Pani, Testing the nature of dark compact objects: A status report, *Living Rev. Relativity* **22**, 4 (2019).
- [27] R. Dey, S. Chakraborty, and N. Afshordi, Echoes from braneworld black holes, *Phys. Rev. D* **101**, 104014 (2020).
- [28] E. Maggio, P. Pani, and G. Raposo, Testing the nature of dark compact objects with gravitational waves, *arXiv*: 2105.06410.
- [29] H. A. Buchdahl, General relativistic fluid spheres, *Phys. Rev.* **116**, 1027 (1959).
- [30] N. Dadhich and S. Chakraborty, Buchdahl compactness limit for a pure Lovelock static fluid star, *Phys. Rev. D* **95**, 064059 (2017).
- [31] A. Alho, J. Natário, P. Pani, and G. Raposo, Compact elastic objects in general relativity, *Phys. Rev. D* **105**, 044025 (2022); **105**, 129903(E) (2022).
- [32] A. Alho, J. Natário, P. Pani, and G. Raposo, Compactness bounds in general relativity, *Phys. Rev. D* **106**, L041502 (2022).
- [33] Z. Mark, A. Zimmerman, S. M. Du, and Y. Chen, A recipe for echoes from exotic compact objects, *Phys. Rev. D* **96**, 084002 (2017).
- [34] C. Posada, Slowly rotating supercompact Schwarzschild stars, *Mon. Not. R. Astron. Soc.* **468**, 2128 (2017).
- [35] M. Deliyergiyev, A. Del Popolo, L. Tolos, M. Le Delliou, X. Lee, and F. Burgio, Dark compact objects: An extensive overview, *Phys. Rev. D* **99**, 063015 (2019).
- [36] R. Dey, S. Biswas, and S. Chakraborty, Ergoregion instability and echoes for braneworld black holes: Scalar, electromagnetic, and gravitational perturbations, *Phys. Rev. D* **103**, 084019 (2021).
- [37] E. Maggio, V. Cardoso, S. R. Dolan, and P. Pani, Ergoregion instability of exotic compact objects: Electromagnetic and gravitational perturbations and the role of absorption, *Phys. Rev. D* **99**, 064007 (2019).
- [38] A. Maselli, P. Pani, V. Cardoso, T. Abdelsalhin, L. Gualtieri, and V. Ferrari, From micro to macro and back: Probing near-horizon quantum structures with gravitational waves, *Classical Quantum Gravity* **36**, 167001 (2019).
- [39] V. Cardoso, A. S. Miranda, E. Berti, H. Witek, and V. T. Zanchin, Geodesic stability, Lyapunov exponents and quasinormal modes, *Phys. Rev. D* **79**, 064016 (2009).

- [40] S. H. Volkel and K. D. Kokkotas, Wormhole potentials and throats from quasi-normal modes, *Classical Quantum Gravity* **35**, 105018 (2018).
- [41] S. Biswas, M. Rahman, and S. Chakraborty, Echoes from braneworld wormholes, *Phys. Rev. D* **106**, 124003 (2022).
- [42] E. Franzin, S. Liberati, J. Mazza, R. Dey, and S. Chakraborty, Scalar perturbations around rotating regular black holes and wormholes: Quasinormal modes, ergoregion instability, and superradiance, *Phys. Rev. D* **105**, 124051 (2022).
- [43] M. Visser, *Lorentzian Wormholes: From Einstein to Hawking*, *Computational and Mathematical Physics* (American Institute of Physics, New York, USA, 1995).
- [44] M. S. Morris and K. S. Thorne, Wormholes in space-time and their use for interstellar travel: A tool for teaching general relativity, *Am. J. Phys.* **56**, 395 (1988).
- [45] S. Kar, S. Lahiri, and S. SenGupta, Can extra dimensional effects allow wormholes without exotic matter?, *Phys. Lett. B* **750**, 319 (2015).
- [46] V. Cardoso and P. Pani, The observational evidence for horizons: From echoes to precision gravitational-wave physics, *Nat. Astron.* **1**, 586 (2017).
- [47] Z. Zhong, V. Cardoso, and E. Maggio, Instability of ultra-compact horizonless spacetimes, *Phys. Rev. D* **107**, 044035 (2023).
- [48] S. Biswas, Massive scalar perturbation of extremal rotating braneworld black hole: Superradiant stability analysis, *Phys. Lett. B* **820**, 136597 (2021).
- [49] P. Bueno, P. A. Cano, F. Goelen, T. Hertog, and B. Vercnocke, Echoes of Kerr-like wormholes, *Phys. Rev. D* **97**, 024040 (2018).
- [50] V. Cardoso, E. Franzin, and P. Pani, Is the gravitational-wave ringdown a probe of the event horizon?, *Phys. Rev. Lett.* **116**, 171101 (2016).
- [51] P. Dutta Roy and S. Kar, Generalized Hayward spacetimes: Geometry, matter, and scalar quasinormal modes, *Phys. Rev. D* **106**, 044028 (2022).
- [52] K. A. Bronnikov and R. A. Konoplya, Echoes in brane worlds: Ringing at a black hole–wormhole transition, *Phys. Rev. D* **101**, 064004 (2020).
- [53] K. A. Bronnikov, R. A. Konoplya, and T. D. Pappas, General parametrization of wormhole spacetimes and its application to shadows and quasinormal modes, *Phys. Rev. D* **103**, 124062 (2021).
- [54] V. De Falco, E. Battista, S. Capozziello, and M. De Laurentis, General relativistic Poynting-Robertson effect to diagnose wormholes existence: Static and spherically symmetric case, *Phys. Rev. D* **101**, 104037 (2020).
- [55] V. De Falco, M. De Laurentis, and S. Capozziello, Epicyclic frequencies in static and spherically symmetric wormhole geometries, *Phys. Rev. D* **104**, 024053 (2021).
- [56] V. De Falco, E. Battista, S. Capozziello, and M. De Laurentis, Testing wormhole solutions in extended gravity through the Poynting-Robertson effect, *Phys. Rev. D* **103**, 044007 (2021).
- [57] V. De Falco, E. Battista, S. Capozziello, and M. De Laurentis, Reconstructing wormhole solutions in curvature based extended theories of gravity, *Eur. Phys. J. C* **81**, 157 (2021).
- [58] V. De Falco, Epicyclic frequencies in the equatorial plane around stationary and axially symmetric wormhole geometries, *Phys. Rev. D* **108**, 024051 (2023).
- [59] V. C. Rubin and W. K. Ford, Rotation of the Andromeda Nebula from a spectroscopic survey of emission regions, *Astrophys. J.* **159**, 379 (1970).
- [60] L. L. Cowie, M. Henriksen, and R. Mushotzky, Are the virial masses of clusters smaller than we think?, Technical Report No. N-87-18481; NASA-TM-89268; NAS-1.15:89268TRN: 87-019139, National Aeronautics and Space Administration, Greenbelt, MD (USA), 1986.
- [61] A. Borriello and P. Salucci, The dark matter distribution in disk galaxies, *Mon. Not. R. Astron. Soc.* **323**, 285 (2001).
- [62] M. Persic, P. Salucci, and F. Stel, The universal rotation curve of spiral galaxies: 1. The dark matter connection, *Mon. Not. R. Astron. Soc.* **281**, 27 (1996).
- [63] U. G. Briel and J. P. Henry, An x-ray temperature map of Coma, [arXiv:astro-ph/9711237](https://arxiv.org/abs/astro-ph/9711237).
- [64] J. K. Adelman-McCarthy *et al.* (SDSS Collaboration), The fourth data release of the Sloan digital sky survey, *Astrophys. J. Suppl. Ser.* **162**, 38 (2006).
- [65] D. Clowe, M. Bradac, A. H. Gonzalez, M. Markevitch, S. W. Randall, C. Jones, and D. Zaritsky, A direct empirical proof of the existence of dark matter, *Astrophys. J. Lett.* **648**, L109 (2006).
- [66] K. Freese, Review of observational evidence for dark matter in the Universe and in upcoming searches for dark stars, *EAS Publ. Ser.* **36**, 113 (2009).
- [67] V. Cardoso, K. Destounis, F. Duque, R. P. Macedo, and A. Maselli, Black holes in galaxies: Environmental impact on gravitational-wave generation and propagation, *Phys. Rev. D* **105**, L061501 (2022).
- [68] L. Hernquist, An analytical model for spherical galaxies and bulges, *Astrophys. J.* **356**, 359 (1990).
- [69] R. A. Konoplya and A. Zhidenko, Solutions of the Einstein equations for a black hole surrounded by a galactic halo, *Astrophys. J.* **933**, 166 (2022).
- [70] A. Einstein, On a stationary system with spherical symmetry consisting of many gravitating masses, *Ann. Math.* **40**, 922 (1939).
- [71] J. C. Feng, S. Chakraborty, and V. Cardoso, Shielding a charged black hole, *Phys. Rev. D* **107**, 044050 (2023).
- [72] S. Kanno and J. Soda, Radion and holographic brane gravity, *Phys. Rev. D* **66**, 083506 (2002).
- [73] R. Casadio, A. Fabbri, and L. Mazzacurati, New black holes in the brane world?, *Phys. Rev. D* **65**, 084040 (2002).
- [74] K. A. Bronnikov and A. V. Michtchenko, Black holes and wormholes in RS2 type brane worlds, *Int. J. Mod. Phys. A* **20**, 2256 (2005).
- [75] K. A. Bronnikov and S.-W. Kim, Possible wormholes in a brane world, *Phys. Rev. D* **67**, 064027 (2003).
- [76] T. Damour and S. N. Solodukhin, Wormholes as black hole foils, *Phys. Rev. D* **76**, 024016 (2007).
- [77] J. F. Navarro, C. S. Frenk, and S. D. M. White, The structure of cold dark matter halos, *Astrophys. J.* **462**, 563 (1996).
- [78] D. V. Gal'tsov and K. V. Kobialko, Photon trapping in static axially symmetric spacetime, *Phys. Rev. D* **100**, 104005 (2019).

- [79] M. Kato and I. Hachisu, Theoretical light curve models of the symbiotic nova CN Cha—Optical flat peak for three years, *Astrophys. J.* **951**, 128 (2023).
- [80] K. V. Kobialko and D. V. Gal'tsov, Photon regions and umbilic conditions in stationary axisymmetric spacetimes: Photon regions, *Eur. Phys. J. C* **80**, 527 (2020).
- [81] I. Bogush, K. Kobialko, and D. Gal'tsov, Killing tensors in foliated spacetimes and photon surfaces, in *Proceedings of the 16th Marcel Grossmann Meeting on Recent Developments in Theoretical and Experimental General Relativity, Astrophysics and Relativistic Field Theories* (World Scientific, Singapore, 2021), [arXiv:2110.04608](https://arxiv.org/abs/2110.04608).
- [82] K. Kobialko and D. Gal'tsov, Photon regions in stationary axisymmetric spacetimes and umbilic conditions, in *Proceedings of the 16th Marcel Grossmann Meeting on Recent Developments in Theoretical and Experimental General Relativity, Astrophysics and Relativistic Field Theories* (World Scientific, Singapore, 2021), [arXiv:2110.04610](https://arxiv.org/abs/2110.04610).
- [83] A. B. Yassine and J. Trlifaj, Flat relative Mittag-Leffler modules and Zariski locality, [arXiv:2208.00869](https://arxiv.org/abs/2208.00869).
- [84] N. Dadhich, S. Kar, S. Mukherji, and M. Visser, $R = 0$ spacetimes and self-dual Lorentzian wormholes, *Phys. Rev. D* **65**, 064004 (2002).
- [85] R. Casadio, A. Fabbri, and L. Mazzacurati, New black holes in the brane world?, *Phys. Rev. D* **65**, 084040 (2002).
- [86] I. Banerjee, S. Chakraborty, and S. SenGupta, Hunting extra dimensions in the shadow of Sgr A*, *Phys. Rev. D* **106**, 084051 (2022).
- [87] I. Banerjee, S. Chakraborty, and S. SenGupta, Silhouette of M87*: A new window to peek into the world of hidden dimensions, *Phys. Rev. D* **101**, 041301 (2020).
- [88] J. A. Gonzalez, F. S. Guzman, and O. Sarbach, On the instability of charged wormholes supported by a ghost scalar field, *Phys. Rev. D* **80**, 024023 (2009).
- [89] J. A. Gonzalez, F. S. Guzman, and O. Sarbach, Instability of wormholes supported by a ghost scalar field. I. Linear stability analysis, *Classical Quantum Gravity* **26**, 015010 (2009).
- [90] K. A. Bronnikov, L. N. Lipatova, I. D. Novikov, and A. A. Shatskiy, Example of a stable wormhole in general relativity, *Gravitation Cosmol.* **19**, 269 (2013).